

1 **Multiplexed code of navigation variables in anterior limbic areas**

2 Jean Laurens¹, Amada Abrego¹, Henry Cham¹, Briana Popeney¹, Yan Yu¹, Naama Rotem¹, Janna Aarse^{1,2},
3 Eftihia K. Asproдини³, J. David Dickman^{1,4}, Dora E. Angelaki^{1,2}

4 ¹ Department of Neuroscience, Baylor college of Medicine, Houston, Texas, USA.

5 ² Center for Neural Science and Tandon School of Engineering, New York University, NY, USA.

6 ³ Laboratory of Pharmacology, Dpt. of Medicine, School of Health Sciences, University of Thessaly,
7 Larissa, Greece

8 ⁴ Department of Electrical and Computer Engineering, Rice University, Houston, Texas, USA.

10 **Address for correspondence:**

11 Dr. Dora E. Angelaki

12 Email: da93@nyu.edu

13 Center for Neural Science, Meyer 901

14 New York University, NY 10003

16 **Acknowledgements:** Supported by the Simons Collaboration on the Global Brain Grant 542949,
17 DC004260, DC014518 and DC015602.

19 **Abstract**

20 The brain's navigation system integrates multimodal cues to create a sense of position and orientation.
21 Here we used a multimodal model to systematically assess how neurons in the anterior thalamic nuclei,
22 retrosplenial cortex and anterior hippocampus of mice, as well as in the cingulum fiber bundle and the
23 white matter regions surrounding the hippocampus, encode an array of navigational variables when
24 animals forage in a circular arena. In addition to coding head direction, we found that some thalamic
25 cells encode the animal's allocentric position, similar to place cells. We also found that a large fraction of
26 retrosplenial neurons, as well as some hippocampal neurons, encode the egocentric position of the
27 arena's boundary. We compared the multimodal model to traditional methods of head direction tuning
28 and place field analysis, and found that the latter were inapplicable to multimodal regions such as the
29 anterior thalamus and retrosplenial cortex. Our results draw a new picture of the signals carried and
30 outputted by the anterior thalamus and retrosplenial cortex, offer new insights on navigational variables
31 represented in the hippocampus and its vicinity, and emphasize the importance of using multimodal
32 models to investigate neural coding throughout the navigation system.

33

Introduction

34 One of the most striking properties of the rodent navigation system is the existence of characteristic cell
35 populations that represent well-defined navigation variables. For instance, place cells are pyramidal
36 neurons in the hippocampus (O'Keefe 1971, 1996) that encode the animal's allocentric position, and
37 head direction (HD) cells in the antero-dorsal thalamic nuclei form a neuronal compass (Taube et al.
38 1995; Blair and Sharp 1996; Zugaro et al. 2001; Peyrache et al. 2015,2017; Page et al. 2017). Place cells
39 and HD cells are thought the prominent neuron types in these regions, where no other navigational
40 variables have been reported. In contrast, other regions such as the medial entorhinal cortex (MEC)
41 encode multiple navigation variables and, as revealed by a recent study (Hardcastle et al. 2017),
42 individual neurons often encode multiple variables. May this be a property exclusively for the MEC, or
43 does mixed selectivity represent a generic property throughout the rodent spatial navigation circuit?

44 Here we used a Linear-Nonlinear (LN) model (Hardcastle et al. 2017) to characterize population
45 responses in a network of brain regions involved in navigation. We first describe neurons in the anterior
46 thalamic nuclei (ATN), and in particular the antero-dorsal thalamic nuclei, and whether they may encode
47 spatially modulated variables other than head direction. We also test for the first time whether neuronal
48 firing is phase-locked to theta-band LFP, a property that has never been reported for head direction cells
49 (HDC) in the antero-dorsal thalamus, yet is frequent in antero-ventral thalamic nuclei HDC (Tsanov 2010,
50 2011).

51 Next, we compare neural selectivity in ATN and the retrosplenial cortex (RSC), noting few similarities.
52 Unlike the ATN, we find that RSC is dominated by the coding of arena boundaries in an egocentric frame
53 of reference (Alexander et al. 2019; Hinman et al. 2019; Gofman et al. 2019; see also Peyrache et al.
54 2017; Wang et al. 2018; Derdikman, 2009). We also characterized neuronal responses in anterior parts
55 of the hippocampal formation (CA2/CA3). Furthermore, we also used the LN model to re-analyze
56 previously published neuronal data recorded in the ATN (Peyrache et al. 2015). Finally, in order to test
57 whether the multiplexed code is communicated among brain areas, we also describe response
58 properties from the cingulum fiber bundle, in the vicinity of Bregma, i.e. at a location where it conveys
59 output fibers from the ATN and RSC (Domesick 1970; van Groen and Vyss 1990,1995, Bubb et al. 2017,
60 2018).

61 Traditional classification methods evaluate a cell's response to a specific navigation variable by
62 computing the corresponding tuning curve, without considering other variables. We found that these
63 approaches produce biased results. In particular, head direction or egocentric boundary tuning is often
64 mistaken for allocentric position tuning; to such an extent that attempting to detect place cells in the
65 anterior thalamus or retrosplenial cortex by computing traditional "place fields" would result in
66 excessive numbers of false positives. This stresses out the importance of using multiplexed models to
67 systematically investigate brain regions where multiple variables are encoded.

68

Results

69 We used tetrodes bundles to record extracellularly while mice (n=22) foraged in a circular arena (50 cm
70 diameter; 8-minutes recording sessions) (**Fig. 1A**). We sampled 5 different brain regions (**Fig. 1B**): the

71 anterior nuclei of the thalamus (ATN, n=7 animals), which included predominantly of recordings in the
72 antero-dorsal nuclei; the retrosplenial cortex (RSC, n=4 animals); the cingulum fiber bundle (n=7
73 animals); the anterior portion of the hippocampus (CA2/CA3; n=3 animals); and the white matter region
74 anterior to the hippocampus (Fimbria and fornix; n=6 animals). Multiple regions were sampled
75 sequentially in some animals. Recording locations were verified post-mortem (**Fig. 1C**, see also **Fig. 6-10**
76 **S1**). We recorded and analyzed the responses of 1219 neurons (300 in ATN, 180 in RSC, 380 in the
77 cingulum, 112 in hippocampus, and 247 in the fimbria).

78 We used a multivariate linear-nonlinear (LN) model (Hardcastle et al. 2017) to test whether each cell
79 responds significantly to a series of navigational variables (**Fig. 2A**), and to assess whether it is
80 modulated by theta-band (5-12 Hz) LFP. Specifically, we tested the 4 variables considered in (Hardcastle
81 et al. 2017): the animal's allocentric position (AP), head direction (HD) and linear speed (LS) in the
82 environment, as well as the phase of the theta-band LFP rhythm (Θ P), and added two additional
83 variables: the egocentric position of the arena's boundary relative to the head (EB) and the head's
84 angular speed (AS). The LN model assumes that multiple variables influence the cell's response in a
85 multiplicative manner and uses an optimization procedure to compute each variable's tuning curve to
86 match the recorded firing rate, as shown next. To determine the best model, each cell's response is
87 fitted separately by each model variable alone, or with pairs of variables (or triplets, and so on) and uses
88 a forward search procedure to determine which variables influence the cell's firing significantly
89 (according to the Log-likelihood ratio; see Methods).

90 **Example cells**

91 We first use two well-known neuron types to illustrate the robustness of the model: an example HD cell
92 recorded in the ATN (**Fig. 3**); and an example hippocampal place cell (AP response) that also fired in
93 phase with theta-LFP (Θ P modulation) (**Fig. 4**). Subsequently, we also illustrate examples of a novel cell
94 type in RSC (**Fig. 5**), as well as coding for more multiplexed variables in other cell types.

95 *ATN example cell:* The example HD cell fired in intense bursts when the head faced a specific allocentric
96 direction (50°; **Fig. 3A,C**, black). We separated HD in 18 bins and computed the average firing rate within
97 each bin. The resulting tuning curve (**Fig. 3B**) was typical of an ATN HD cell, exhibiting a sharp peak with
98 an average firing of 104 spk/s at the preferred direction. Computing a HD tuning curve in this manner
99 (the 'experimental' tuning curve) is the traditional approach for evaluating HD responses, typically
100 combined with a shuffling-based statistical analysis of the curve's tuning amplitude. By contrast, the LN
101 model fits a tuning curve and uses a cross-validation procedure to test for statistical significance. In this
102 cell, the 'reconstructed' tuning curve (**Fig. 3D**) resembles the experimental tuning curve (**Fig. 3C**).

103 To evaluate the set of variables encoded by this cell, we first fitted the firing rate based on each of the 6
104 variables individually (**Fig. 3E**, left). HD provided a considerably better fit, measured by the Log-
105 likelihood ratio, than any other variable, and was selected as the best first-order model. Next, we tested
106 for all 2nd order models by adding one of the 5 remaining variables to HD (**Fig. 3E**, middle). None of these
107 models provided a significant increase in fit quality compared to HD alone. Therefore, the model
108 selection procedure was terminated, and the HD model was selected as the best fitting. The full model

109 including all 6 variables (shown for reference in **Fig. 3E**, right) did not provide a significantly better fit
110 than the HD model alone.

111 To quantify tuning strength, we developed a ‘normalized tuning amplitude (NTA)’, which is equal to the
112 curve’s trough to peak amplitude divided by the peak firing rate (i.e. the maximum value across the
113 ‘reconstructed’ tuning curves of all variables). For this particular example cell, firing rate varied from
114 practically zero (1 spk/s) to a peak of (104 spk/s), resulting in a NTA of 0.99.

115 *Hippocampal place (AP) cell:* For an example hippocampal cell that responded to AP and was modulated
116 by Θ P, the model selection process is illustrated in **Fig. 4A**. Here, adding Θ P to the best 1st order model
117 (AP) increased the fitting quality significantly. None of the 3rd order models that included AP and Θ P
118 provided a significantly better fit than the AP+ Θ P model, which was therefore selected as a best-fitting
119 model.

120 The cell’s AP and Θ P response properties are summarized in **Fig. 4B,C**. When the animal explored its
121 environment randomly, neuronal firing occurred preferentially in the lower right portion of the arena
122 (**Fig. 4B**, left). An AP tuning curve, computed by following the usual approach of binning neuronal
123 spiking, exhibited a place field at the corresponding position (**Fig. 4B**, middle). The fitted tuning curve
124 constructed by the LN model resembled the experimental curve (**Fig. 4B**, left; note that it is smoother
125 due to the LN model’s smoothness constraint; see Methods). The cell’s firing decreased from a peak 10
126 spk/s to a minimum of 1 spk/s, and accordingly the curve’s NTA was 0.9. The cell was phase-locked with
127 the LFP, as shown by the fitted Θ P tuning curve (**Fig. 4C**) with a NTA of 0.57. The simulated firing rate
128 (**Fig. 4D**, red), computed based on the AP and Θ P tuning curve, followed the cell’s measured firing well
129 (**Fig. 4D**, black).

130 *Egocentric boundary cell in RSC:* The LN model incorporated a variable defined as the egocentric position
131 of the arena’s boundary (EB). Because the arena used in the present experiments is circular, knowing
132 the egocentric location of the entire boundary is equivalent to knowing the egocentric location of its
133 closest point (**Fig. 5A,B**), which may be positioned anywhere within 25 cm of the head (**Fig. 5B**; see
134 **Suppl. Fig. 1** for details). How the LN model fits the responses of an example RSC cell with EB tuning is
135 shown in **Fig. 5C,D** (see also **Suppl. Movie 1**). This cell was largely multimodal (**Fig. 5C**): its firing rate (**Fig.**
136 **5D**) was affected significantly by head direction and linear as well as angular speed (HD, EB, LS, **Fig. 5E**),
137 in addition to EB (**Fig. 5F**). Nevertheless, the EB response was by far the most predominant (NTA=0.96
138 versus NTA \leq 0.17 for all other significant variables).

139 The preferred EB response occurred in close proximity to the arena’s boundary *while* facing directly
140 towards it, i.e. when the boundary was directly in front of the head (**Fig. 5F**, left; **Suppl. Movie 1**). In
141 contrast, the cell was virtually silent when the animal faced away from the boundary, even when it was
142 in close proximity (**Fig. 5F**, left; **Suppl. Movie 1**). Furthermore, the firing was independent of the animal’s
143 allocentric location, i.e. the cell could fire anywhere along the boundary, as long as the animal was
144 facing it. Both the experimental and fitted tuning curves exhibited a sharp peak at the corresponding
145 location (**Fig. 5F**, middle and right panels). Note that, due to its EB tuning, the cell fired more on average
146 when the animal’s allocentric position (AP) was close to the arena’s boundary (**Fig. 5G**). This is apparent

147 on the *experimental* AP tuning curve, which is computed directly from experimental data (**Fig. 5G**,
148 **middle**). Nevertheless, the model revealed that the cell was not sensitive to allocentric position, and the
149 *fitted* AP tuning curve was flat.

150 Overview of population responses

151 *Anterior thalamic nuclei*

152 We targeted the antero-dorsal nuclei of the thalamus in 7 animals (**Fig. 6**). Histological localization of the
153 electrode tracks (**Suppl. Fig. 2A**) confirmed that most recordings sites were indeed located in these
154 nuclei. Yet, we can't exclude that some tetrodes may have contacted neighboring nuclei (e.g. antero-
155 ventral or latero-dorsal). Therefore, we refer to these recorded regions as anterior thalamic nuclei
156 (ATN). The proportions of cells characterized as predominantly APC, EBC, HDC, LSC and ASC are shown in
157 **Fig. 6A**. Non-spatially modulated cells are represented by the white area of the chart, and the
158 population of Θ -modulated cells is outlined in black in each sector. The proportions of cells significantly
159 modulated by any one of the 7 variables are shown as a histogram in **Fig. 6B**. Each bar is broken down
160 into colored segments that represent the predominant variable (e.g., the variable with the highest NTA).
161 Population responses recorded in individual animals are shown in **Suppl. Fig. 2**.

162 As expected, we found that approximately half (46%) - of ATN cells are HDC, that is, HD is the variable
163 that modulates the cell's firing rate the strongest (**Fig. 6A**). A small fraction of cells exhibited stronger
164 selectivity to another variable, typically AP (12%), EB (5%) or LS (3%) (**Fig. 6A,B**, green, blue and yellow
165 bars). Across the population, the total fraction of HD-tuned ATN cells was 51% (**Fig. 6B**). HD responses
166 typically had very high NTA (**Fig. 6C**, orange; median across all cells with significant HD tuning = 0.87, 1st-
167 9th deciles: 0.47-0.98).

168 The peak firing rate of HDC varied widely (1st-9th decile: 6-85 spk/s; median: 20 spk/s; **Fig. 6D**). In
169 particular, a large cluster of HDC located in the upper right corner of **Fig. 6D** exhibited vigorous and
170 specific firing (peak >30 spikes/s; NTA \approx 1), which is generally associated with "typical" HDC.
171 Nevertheless, we also encountered a number of ATN HDC with lower peak responses.

172 The second spatial variable represented in the ATN was allocentric position; 19% of ATN cells had
173 significant AP responses; **Fig. 6B**), and NTA could reach high values (median = 0.6, 1st-9th deciles: 0.27-
174 0.88, **Fig. 6C**, see example cells in **Suppl. Fig. 3**). A smaller proportion (10%) of ATN cells encoded
175 egocentric boundary (**Fig. 6B**), with substantial NTA (median = 0.58; **Fig. 6C**), and 5% were classified as
176 EBC (**Fig. 6A**). A small proportion (9%) of ATN cells were tuned to linear speed, and 3% were identified as
177 LSC (**Fig. 6A,B**, orange). Nevertheless, linear speed responsiveness was modest (median NTA=0.22; **Fig.**
178 **6C**). Angular speed responsiveness was rare (6%) in ATN, and only 2 cells (<1%) were predominantly
179 tuned to AS (**Fig. 6A-C**, violet).

180 About half (47%) of ATN cells were modulated by Θ . Theta phase modulation was most prominent
181 among APC, EBC and LSC (78%), compared to HDC (53%) (**Fig. 6A**). Despite the presence of a theta
182 rhythm in all animals (**Suppl. Fig. 2**), there was a marked inter-animal variability in the fraction of Θ -

183 modulated HDC: almost all spatially-modulated cells in animals H51M, H54M and I29M, but almost none
184 in animals H71M, H72M and I10M3.

185 APC and EBC exhibited comparable range of firing as HDC: APC: median = 18 spk/s, 1st-9th deciles: 6-68;
186 EBC: median = 15 spk/s, 1st-9th deciles: 6-54. Thus, in summary, the 3 main classes of spatially tuned ATN
187 neurons (HDC, APC and EBC) could exhibit specific responses (e.g. NTA>0.6; **Fig. 6D**) with occasionally
188 vigorous peak responses (e.g. close to 100 spk/s, **Fig. 6D**), although lower peak responses could also be
189 encountered (e.g. <10spk/s, **Fig. 6D**).

190 We also quantified additional response parameters. The neuronal firing properties (mean firing rate,
191 CV2 and spike duration) of ATN neurons were broadly distributed (**Fig. 6E,F**): average firing rate ranged
192 from 1.5 to 27 spk/s (1st-9th decile; median=7 spk/s) and CV2 from 0.7 to 1.27 (1st-9th decile; median
193 0.98). Firing rate and CV2 were inversely correlated (**Fig. 6E**; Spearman rank correlation=-0.75, $p<10^{-10}$).
194 The trough to peak duration of action potentials followed a bimodal distribution (**Fig. 6F**), thus neurons
195 could be separated in clearly distinct groups of short-duration (trough to peak ≤ 0.33 ms, 49%) and long-
196 duration (trough to peak > 0.33 ms, 51%) spikes. Neurons with short and long spike duration had similar
197 mean firing rate (7 vs 7 spk/s, $p=0.3$, Wilcoxon rank test) and slightly different CV2 (0.94 vs 1.02, $p=10^{-3}$).
198 A further examination (**Suppl. Fig. 2**) revealed inter-subject differences in firing properties: cells in
199 animals H51M, H54M and H59M were generally low-firing and more irregular and were distributed
200 between short and long-duration spikes, whereas cells in animals H71M, H72M and I10M3 had higher
201 firing rates, were more regular and had predominantly low spike duration.

202 Note that we could not identify any differences in variable coding among narrow and broad spiking
203 neurons. HD cells could exhibit short or long-duration spikes (short- vs long-duration: 86 vs 51 cells, i.e.
204 63% vs 37%). The two groups exhibited similar mean firing rate (median: 7.3 vs 9.3 spk/s, $p=0.6$,
205 Wilcoxon rank test; **Fig. 6E**) and CV2 (median: 0.92 vs 1, $p=0.07$). However, HDC with short-duration
206 spikes had larger NTA (median = 0.92 vs 0.81, $p=3.10^{-5}$) although similar peak firing (23 vs 17 spk/s,
207 $p=0.24$). We also tested whether narrow and broad spiking neurons were most likely to be Θ -
208 modulated. To avoid a confounding factor due to inter-animal variability (where neurons H71M, H72M
209 and I10M3 are rarely Θ -modulated and generally narrow-spiking), we limited this analysis to H51M,
210 H54M, H59M and I29M, and excluded non-spatially modulated neurons. We found that narrow and
211 broad spiking neurons were equally likely to be Θ -modulated (Chi-Square test, $\chi^2=0.36$, $n= 1$ d.o.f,
212 $p=0.54$).

213 ***Additional ATN recordings (Peyrache et al. 2015)***

214 In order to corroborate our finding that populations of neurons in the ATN encode AP, we analyzed
215 previous recordings published in Peyrache et al. 2015 (**Suppl. Fig. 4,5**). Population responses (**Suppl. Fig.**
216 **4**) were similar as in our recordings, and in particular we found substantial fractions of APC in 2 out of 6
217 animals (**Suppl. Fig. 5**). Peyrache et al. (2015) used probe arrays (8 shanks, 200 μ m spacing), which
218 allowed us to investigate the spatial distribution of APC and HDC (**Suppl. Fig. 5**). We found that APC tend
219 to be distributed more laterally than HDC, although the two populations overlap (**Suppl. Fig. 5C**).
220 Furthermore, HDC and APC cells recorded in Peyrache et al. 2015 generally cover three probe shanks

221 (Suppl. Fig. 5A,B), which span 400 μm laterally. Since the extent of the antero-dorsal nuclei is at most
222 400 μm , it is unlikely that all 3 shanks were in this nucleus; and the most lateral of the 3 shanks may
223 have been in an adjacent nucleus (antero-ventral or latero-dorsal). In our study, recordings that
224 identified APC in the ATN were restricted to a single track (since we used one tetrode bundle) and a
225 narrow range of depth (Suppl. Fig. 5I-K), and histology indicated that tetrode tracks were located in the
226 antero-dorsal nuclei (Suppl. Fig. 3A). Collectively these results suggest that APC exist in at least some
227 portions of the antero-dorsal nuclei, although they may be more numerous in the adjacent antero-
228 ventral or latero-dorsal nuclei.

229 *Retrosplenial cortex*

230 We implanted four animals for recording in the RSC (Fig. 7). One implantation (animal AA2) reached the
231 granular cortex, where 119/180 neurons were recorded (Fig. 7). The other implantations (animal AA1,
232 AA18, AA20) reached the dysgranular cortex. Responses from these regions were similar (Suppl. Fig. 6),
233 thus pooled in Fig. 7.

234 By far, the variable represented in RSC the most was egocentric boundary (see Alexander et al. 2019).
235 About half (45%) of RSC cells were classified as EBC. EB responses exhibited large NTA (median = 0.7; 1st-
236 9th decile: 0.53-0.88; Fig. 7A-C; an example EBC is shown in Fig. 5 and Suppl. Movie 1). Peak firing rates
237 (Fig. 7D) were clustered around a median value of 7 spk/s (1st-9th decile: 17-48). We found that the
238 'preferred boundary position' of EBC (i.e. the egocentric boundary position at which their firing was
239 maximal Suppl. Fig. 7A) is generally located close to the head (median = 4.95 cm, CI = [4.03-5.8]; Suppl.
240 Fig. 7B). In contrast, the egocentric bearing was distributed uniformly (Suppl. Fig. 7C), indicating that
241 EBC could respond when the boundary was in front of the head (Suppl. Fig. 7A,C: Front; F), to the right,
242 left (R/L in Suppl. Fig. 7C), or behind the head (Suppl. Fig. 7A,C: Behind; B).

243 A sizeable fraction of EBC (52%) were significantly tuned to HD (Fig. 7B; blue portion of the bar 'HD'), but
244 with modest NTA (median = 0.27, 1st-9th decile: 0.13-0.41; Fig. 7B). Likewise, 22% of EBC were tuned to
245 AS (median NTA = 0.27; 1st-9th decile: 0.14-0.48) and 15% were tuned to LS (median NTA = 0.25; 1st-9th
246 decile: 0.08-0.5). This indicates that EBC were often multimodal. It is striking that the majority of cells
247 that exhibited significant HD tuning were in fact EBC.

248 Beyond EBC, only small fractions of responsive cells were encountered. Only 4% of the population was
249 classified as HDC (Fig. 7A), although, as mentioned above, many EBC exhibited significant HD responses.
250 Interestingly, a few (n=5, 3%) ASC were identified, and these cells had large NTA (higher than 0.8 in 4
251 cells; Fig. 7D, magenta). LFP recorded in the RSC exhibited a clear theta rhythm (Suppl. Fig. 6). Yet, ΘP
252 responses were practically non-existent.

253 In general, RSC cells fired in a homogenous and tightly clustered fashion (Fig. 7E): the average firing rate
254 was distributed around a median of 8.3 spk/s and ranged from 2.7 to 26 spk/s (1st-9th decile). The CV2
255 was distributed around a median of 0.84 and ranged from 0.65 to 0.98. Most neurons (145/180, 81%)
256 had long-duration spikes (Fig. 7F).

257 *Cingulum fiber bundle*

258 We recorded neuronal activity from the cingulum bundle (**Suppl. Fig. 8,9**). Most recordings (all animals
259 except AAO; **Suppl. Fig. 9**) were located near Bregma, i.e. at the level of the transition between cingular
260 and retrosplenial cortex along the antero-posterior axis. At this level, the cingulum conveys projections
261 from the anterior thalamus and RSC. Therefore, we hypothesized that we would record a majority of
262 units with short-duration spikes, consistent with axonal spikes (Barry 2015), whose firing and response
263 properties resembled a mixture of ATN and RSC neurons. In agreement with this hypothesis, 23% of cells
264 were classified as HDC (**Suppl. Fig. 8A,B**) and 18% as EBC (**Suppl. Fig. 8A,B**). As expected, the majority of
265 neurons (300/380, 79%) had short-duration spikes (**Suppl. Fig. 8F**). These results show that tetrode
266 recording from the cingulum fibers bundles are possible (and, in fact, remarkably easy); and that the
267 section of cingulum we recorded likely conveys fibers projecting from the ATN and RSC.

268 ***Postsubiculum***

269 We also analyzed previously published data recorded by Peyrache et al. (2015) in the postsubiculum of
270 three mice (**Suppl. Fig. 10**). We found a large fraction (31%) of HDC (**Suppl. Fig. 10A**), with low or
271 moderate firing rates (**Suppl. Fig. 10D,E**) and long spike duration (**Suppl. Fig. 10F**), consistent with layer
272 3 pyramidal neurons (Tukker et al. 2015, Preston-Ferrer et al. 2016, Simonnet et al, 2017; Simonnet et
273 Fricker, 2017). The second most prominent population were APC (14%).

274 ***Classification of HDC: comparison with other techniques***

275 To better appreciate how the LN model compares to classification methods used in previous studies, we
276 evaluated HD tuning in ATN, RSC and cingulum using conventional approaches (**Suppl. Fig. 11**), which
277 classify cells as HD-tuned if the mean vector length $|R|$ of their experimental HD tuning curve pass a
278 shuffling test or an arbitrary threshold (e.g. 0.26, Jacob et al. 2017, or 0.4, Yoder et al. 2009; Kornienko
279 et al. 2018). We found that strongly tuned HD cells that pass a threshold of $|R| \geq 0.26$ are equally well
280 detected by the LN test and other methods. We also found that a shuffling test is more sensitive than
281 the LN model for detecting cells with moderate HD tuning (**Suppl. Fig. 11B**). However, AP or EB tuning
282 can be erroneously interpreted as HD tuning due to sampling non-uniformity (Muller et al. 1994; Cacucci
283 et al. 2004 ; Rubin et al. 2014; **Fig 7S6C**). The LN model is robust to this issue by construction, and a
284 threshold of $|R| > 0.26$ is high enough to rule out such cells. In contrast, using a shuffling test without
285 accounting for AP or EB tuning may produce a moderate number of false positives, which we estimated
286 to be 5-10% of the cells in the regions considered (**Suppl. Fig. 11G-I**). As a conclusion, the LN model is a
287 robust technique for classifying HD cells (as well as other cell types) that agrees well with $|R|$ tests,
288 although it is less sensitive than shuffling tests for cells with low tuning strength.

289 ***Hippocampus***

290 Many studies have focused on pyramidal place cells that are identified based on their long spike
291 duration and typically exhibit AP responses. Here we recorded and classified the responses of a variety
292 of cell types, including cells with short- and long-duration spikes, located mainly in the anterior part of
293 the hippocampus.

294 *AP (place) cells*: A fifth (19%) of hippocampal cells were classified as APC (**Fig. 8A,B**). A significantly large
295 fraction of APC (Chi square test, $\chi^2=11$, 1dof, $p<10^{-3}$) had very long spike duration (large symbols in **Fig.**
296 **8D-F**; 10/21 APC, and 10/23 cells with very long spike duration are APC). APC with very long spike
297 duration had strong NTA (median: 0.87, 1st-9th decile: 0.81-0.93, **Fig. 8D**) and low peak firing (median: 5
298 spk/s, 1st-9th decile: 2.7-11.4, **Fig. 8D**); while other APC had lower NTA (median 0.77, 1st-9th decile: 0.55-
299 0.92, $p=0.012$, **Fig. 8D**) and widely distributed peak firing (median 21 spk/s, 1st-9th decile 2-56 spk/s, **Fig.**
300 **8D**).

301 *LS cells*: One fifth (20%) of cells encoded the animal's linear speed (**Fig. 8A**). LSC could fire short-duration
302 (14/22, 64%) or long-duration (8/22, 36%) spikes (**Fig. 8F**). LS modulation amplitudes were modest
303 (median: 0.37, 1st-9th decile: 0.24-0.59, **Fig. 8C,D**).

304 *Other responses*: We also encountered a substantial (9%) fraction of EBC in the hippocampus **Fig. 8A,B**,
305 with similar modulation amplitudes as in other areas (median: 0.63, 1st-9th decile: 0.51-0.9, **Fig. 8C**).

306 *Theta rhythm*: Theta rhythm was recorded in all animals (**Suppl. Fig. 12**). A large fraction (53%) of all
307 neurons was Θ P modulated, including the majority of APC (86%) and of LSC (95%) (**Fig. 8A**). Modulation
308 amplitude was moderate (media: 0.4, 1st-9th decile: 0.2-0.71) (**Fig. 8C**).

309 *Spiking properties*: As in other regions, there was a negative correlation between mean firing rate and
310 CV2 (**Fig. 8E**, Spearman rank correlation=-0.85, $p<10^{-10}$). Spiking duration varied widely (**Fig. 8F**): 38% of
311 the neuronal population fired short-duration spikes (≤ 0.33 ms trough to peak). Amongst neuron with
312 longer-duration spikes, we observed that a large fraction (21% of the total population) fired very long-
313 duration spikes (>0.9 ms trough to peak), and the remaining 41% fired spikes with intermediate
314 duration. Furthermore, many neurons with >0.9 ms trough to peak spike duration clustered in **Fig. 8E**
315 (large symbols in upper left) in a group characterized by low firing rate (typically less than 4spk/s) and
316 highly irregular (CV2 >1.2).

317 ***Fimbria and fornix***

318 We recorded neuronal responses in white matter regions located anterior and ventral to the
319 hippocampus. These regions encompass the fimbria and fornix, and convey many fibers between
320 regions of the navigation circuit (Adelmann et al. 1996; Bubb et al. 2017). Accordingly, we found that
321 neurons recorded in these regions encode a variety of navigation variables (**Suppl. Fig. 13, Suppl. Fig.**
322 **14**).

323 **Preferred phase of Θ P-modulated cells**

324 We found that the preferred phase of Θ P-modulated cells were consistent across areas, with preferred
325 firing occurring preferentially in the descending phase (i.e. between 180° and 270°, **Suppl. Fig. 15**).

326 ***Classification of APC: comparison with other techniques***

327 We also compared the LN model to previous techniques (Skaggs 1993; Rubin et al. 2014) that compute
328 the spatial information (SI) or AP tuning curve and use a shuffling test to evaluate statistical significance

329 **(Suppl. Fig. 16)**. Again we found that the LN model is less sensitive than the shuffling test **(Suppl. Fig.**
330 **16B)**. Furthermore, we found that HD tuning could easily be misinterpreted as AP tuning, as pointed out
331 by (Peyrache et al. 2017) **(Suppl. Fig. 16C**, left), an issue that could also affect EBC **(Suppl. Fig. 16C**,
332 right). Because of this, 17 to 24% of the cell populations in ATN, RSC and cingulum were incorrectly
333 classified as APC by a conventional shuffling test. Thus, a traditional measure of spatial information
334 combined with a shuffling test may be enough to identify APC reliably in the hippocampus, where EBC
335 and HDC are scarce **(Suppl. Fig. 16K)**. In contrast, testing for AP responses in regions that host other cell
336 types, such as the ATN, RSC, cingulum and parahippocampal regions requires classification methods that
337 can control for responses to other variables, such as the LN model or techniques used in earlier studies
338 (Muller et al. 1994; Cacucci et al. 2004 ; Rubin et al. 2014; Peyrache et al. 2017).

339

340

Discussion

341 We used an LN model (Hardcastle and al. 2017) to analyze how neuronal activity in multiple areas of the
342 brain's navigation network encode combinations of navigation variables. As expected, the LN model
343 identified prominent and well-known characteristics of these areas, such as the prevalence of HDC in
344 ATN and postsubiculum, or place cells in the hippocampus, but also revealed several novel features. We
345 found that egocentric information is represented extensively not only in RSC (Alexander et al. 2019), but
346 also in ATN and hippocampus. Furthermore, ~12% of ATN neurons encode the animal's allocentric
347 position, a finding that we confirmed by re-analyzing previously published data (Peyrache et al. 2015).
348 We recorded spiking activity from the cingulum fiber bundle and found that most units resemble ATN or
349 RSC neurons, suggesting that spatial information encoded in these regions travels along the cingulum.

350 *Anterior thalamic nuclei:* Our recordings in the ATN consisted predominantly of antero-dorsal nuclei
351 neurons. The presence of a large population of HDC in the ATN of rats (Taube et al. 1995; Blair and Sharp
352 1996; Zugaro et al. 2001; Peyrache et al. 2015,2017; Page et al. 2017) and mice (Yoder and Taube 2009)
353 is well documented.

354 More surprising was the finding of a substantial population of APC, i.e. cells tuned to the animal's
355 allocentric position, in 3 of our animals **(Suppl. Fig. 2)** as well as in 2 animals in a previously published
356 dataset (Peyrache et al. 2015; **Suppl. Fig. 5**), some of which exhibited very sharp tuning **(Suppl. Fig. 3)**.
357 Importantly, the spike waveform of most APC exhibited long trough to peak duration (>0.33 ms; **Fig. 6F**
358 and **Suppl. Fig. 4F**, green), indicating that they were not likely fibers traversing the ATN. These APC
359 responses could not have been recorded in the fimbria, just dorsal to the thalamus, and erroneously
360 classified as ATN cells because, although the fimbria contains 12% of APC **(Suppl. Fig. 13A)**, these cells
361 typically exhibit short trough to peak duration **(Suppl. Fig. 13F)**. Yet, we cannot resolve with complete
362 certainty the location of these neurons. The dataset of Peyrache et al. (2015) indicates that these
363 neurons may overlap the population of HDC in the antero-dorsal nuclei, but be more numerous lateral
364 to the antero-dorsal nuclei, i.e. in the antero-ventral or latero-dorsal nuclei **(Suppl. Fig. 5)**. Thus, more
365 detailed studies would be required to assess the spatial distribution of APC in the anterior thalamus.

366 Theta rhythm is a fundamental property of the navigation circuit, thought to mediate memory and
367 planning in the hippocampus (Buzsáki and Moser 2013) and in general inter-regions communication
368 (Maris et al. 2016). Previous studies (Vertes et al. 2001, Albo et al. 2003) have shown that neurons in the
369 ATN, including the antero-ventral and antero-dorsal nuclei, are modulated by the *hippocampal* theta
370 rhythm. Furthermore, Tsanov and colleagues (2010,2011) have shown that a portion of HDC in the
371 antero-ventral nuclei of rats exhibit a rhythmic firing at theta frequency. In this study, we targeted the
372 ATN of 7 animals, and histology (**Suppl. Fig. 2A**) indicates that most recording took place in the antero-
373 dorsal nuclei. We found that a clear theta-band LFP was present in all animals (**Suppl. Fig. 2E**, peak in the
374 5-12Hz frequency range), and that over half of HDC and most APC and EBC were modulated by local
375 theta rhythm. Collectively, these studies indicate that at least part of HDC as well as EBC in the ATN are
376 modulated by a theta rhythm that may originate in the hippocampus. The hippocampal formation
377 projects to the ATN directly, though projections of the subiculum to the antero-ventral nuclei and of the
378 postsubiculum and parasubiculum to the antero-dorsal nuclei. It also projects indirectly via the
379 mammillary nuclei (Kocsis 1997; Vertes et al. 2001; Vann and Aggleton 2004).

380 *Retrosplenial cortex and Egocentric boundary cells:* We found that about half of RSC neurons encode the
381 egocentric position of the arena's boundary. The existence of egocentric boundary cells (EBC) was
382 proposed by Derdikman (2009), and EBC were recently identified in the entorhinal cortex (Wang et al.
383 2018, Gofman et al. 2019), postrhinal cortex (Gofman et al. 2019), parasubiculum (Gofman et al. 2019),
384 striatum (Hinman et al. 2019) and RSC (Alexander et al. 2019). Several studies have described HDC in the
385 RSC (Chen et al. 1994a,b; Cho et al. 2001; Jacob et al. 2017; Lozano et al. 2017). Here we found that,
386 although 28% of RSC cells were tuned to HD, the majority of these were in fact EBC with weaker but
387 significant responses to HD, such that only 4% of RSC cells were classified as HDC. Over half of EBC in the
388 RSC were significantly tuned to HD (similar to EBC in the parasubiculum and medial entorhinal cortex,
389 Gofman et al. 2019), which suggests that the RSC may be involved in combining multiple reference frames
390 (see Clark et al. 2018). Note that the population responses appear similar in the granular (animal AA2;
391 **Suppl. Fig. 6**) and dysgranular (other animals; **Suppl. Fig. 6**) cortices.

392 *Cingulum fiber bundle:* The cingulum connects several areas of the navigation system (Domesick 1970;
393 van Groen and Vyss 1990,1995, Bubb et al. 2017, 2018). It conveys anterior thalamic projections to the
394 RSC and parahippocampal regions and RSC projections to the cingulate cortex and parahippocampal
395 regions. The cingulum also carries projections from the subiculum to the RSC and parahippocampal
396 regions, however it is unlikely that these fibers were recorded since most of our cingulum recordings
397 were performed at the level of the anterior part of the RSC, i.e. ~0.2mm posterior to Bregma. Lesion
398 studies have confirmed that the cingulum is involved in using allocentric cues for spatial navigation (see
399 Bubb et al. 2018 for review), suggesting that it conveys spatial information.

400 The present recordings from the cingulum identified large fractions of HDC and EBC that are strikingly
401 similar to their ATN and RSC counterparts. In particular, many HDC in the cingulum exhibited the high
402 firing rate and NTA (**Suppl. Fig. 9D**) that are typical of ATN HDC (**Fig. 6D**) and would scantily be
403 distinguishable from ATN units when examined online. Likewise, EBC recorded in the cingulum were
404 similar to those encountered in RSC (**Fig. 7D, Suppl. Fig. 9D**), but as expected exhibited shorter
405 waveforms (Robbins, 2013).

406 *Hippocampus*: As expected, we found a population of APC in the hippocampus that matched the typical
407 profile of hippocampal place cells in rats (O'Keefe 1971, 1796) and mice (Muzzio, 2009; Jeantet, 2012;
408 Kinsky, 2018), i.e. high spatial selectivity, low average firing, and long spiking duration (**Fig. 8D-F**). We
409 also recorded a population of cells that were tuned to linear speed. In agreement with a recent study
410 (Góis and Tort 2018), these cells often exhibited fast spiking and short spike durations.

411 *Fimbria and fornix*: Neural activity in the white matter regions located anterior and ventral to the
412 hippocampus, regions that contain a variety of fiber tracks, including projections from the septal nuclei
413 and entorhinal cortex as well as commissural projections (Adelmann et al. 1996; Bubb et al. 2017),
414 showed a variety of spatially modulated signals. In particular, a sizable population (12%) of APC was
415 identified (**Suppl. Fig. 13A**), although its properties were clearly distinct from those of typical
416 hippocampal place cells (**Fig 8A**). Most notable is the fact that 16% of recorded cells were HDC (**Suppl.**
417 **Fig. 13A**) with large firing rate and NTA (**Suppl. Fig. 13D**). In many animals (e.g. H71M, I29M, VR8, **Suppl.**
418 **Fig. 14**), these HDC were recorded directly above the thalamus. This reveals a methodological challenge
419 for targeting ATN, since it shows that lowering electrodes until characteristic HDC are observed is not
420 sufficient because similar response properties are common above the thalamus. Although tetrodes are
421 rarely used to target fibers, previous studies (Robbins et al. 2013) have shown that they can be used to
422 record axonal spikes. We found that spiking could readily (and, in fact, remarkably easily) be recorded in
423 the fiber tracks. Although fiber tracks traveling in the fimbria are difficult to identify, the cingulum is
424 anatomically well delimited, and our study demonstrates that systematic investigations of information
425 transmitted along this bundle is feasible.

426 In summary, the LN model (Harcastle et al. 2018) offers a more robust way to investigate neurons
427 responses recorded in areas of the brain's navigation system by allowing to test for multiple variables at
428 once while proving remarkably immune to pitfalls such as overfitting. In contrast, traditional methods of
429 computing HD tuning curves or place fields often proved impracticable when applied across all brain
430 areas (**Suppl. Fig. 8, Suppl. Fig. 11**): for instance, a traditional place field analysis designed for
431 hippocampal place cells produces aberrant results in the thalamus because it is biased by HD tuning
432 (**Suppl. Fig. 11**). Our study provides a new picture of the information encoded by ATN and RSC cells as
433 well as their output bundle, while re-visiting the responses in the anterior hippocampus and the
434 neighboring white matter areas, and may serve as a guide for future investigations in these areas.

435 **Methods**

436 *Animals*

437 A total of 22 male adult mice (21 C57BL/6; 1 nNOS-ChR2 BAC C57BL/6 transgenic mouse: VR8), 3-6
438 months old, were used in this study. We implanted a head-restraining bar and a microdrive/tetrode
439 assembly under general anesthesia (Isoflurane) and stereotaxic guidance. Animals were single-housed
440 on a reversed [12/12] light/dark cycle. Experimental procedures were conducted in accordance with US
441 National Institutes of Health guidelines and approved by the Animal Studies and Use Committee at
442 Baylor College of Medicine (protocol n°AN-5995).

443 *Neuronal recordings*

444 Neurons were recorded using 6 (animals AA1/AA2/AA18/AA20), 5 (animal VR8) or 4 (all other animals)
445 tetrode bundles constructed with platinum-iridium wires (17 micrometers diameter, polyimide-
446 insulated, California Fine Wire Co, USA) and platinum-plated for a target impedance of 200kΩ using a
447 Nano-Z (Neuralynx, Inc) electrode plater. Tetrodes were cemented to a guide tube (26-gauge stainless
448 steel) and connected to a linear EIB (Neuralynx EIB/36/PTB). The tetrode and guide tube were attached
449 to the shuttle of a screw microdrive (Axona Ltd, St Albans, UK) allowing a travel length of ~5mm into the
450 brain.

451 Tetrodes were positioned under stereotaxic guidance. We targeted the ATN by implanting 0.2mm
452 posterior and 0.7mm lateral relative to Bregma, and placing the tetrodes at an initial depth of 1.8mm
453 relative to the surface of the cortex. The cingulum was targeted by implanting at the same coordinates
454 but at an initial depth of 1.2mm (except for one animal, AA0, where the cingulum was reached 2mm
455 posterior to Bregma). The anterior hippocampus was targeted by implanting 0.6mm posterior and
456 0.7mm lateral relative to Bregma. Recordings in the fimbria were obtained along the track of electrodes
457 targeting the hippocampus, ATN or cingulum. The RSC was targeted by implanting 2mm posterior and
458 0.07mm (AA2/AA18), 0.5mm (AA20) or 0.7mm (AA1) lateral relative to Bregma and placing the
459 electrodes at the surface of the cortex.

460 LFP were recorded as a low-frequency content of the neuronal data, referenced to a ground screw
461 implanted in the skull. Similar to Harcastle et al. 2015, we downsampled LFP data to 250Hz and band-
462 pass filtered it in the 4Hz-12Hz range (second-order Butterworth filter).

463 At the end of the study, the animals underwent transcardial perfusion with 4% paraformaldehyde (PFA).
464 The brains were postfixed in 4% PFA and then transferred to 30% sucrose overnight. Brain sections
465 (40µm) were stained (Nissl or neutral red staining), and examined using bright-field microscopy to
466 localize tetrode tracks.

467 *Recording procedure*

468 We recorded neural activity while animals explored a circular arena (50cm diameter, 30cm height).
469 Recordings were performed in 8-minutes sessions. The walls of the arena were white, with a black cue
470 card covering an angle of 45°. Illumination was provided by a LED strip lining the top of the white section
471 of the arena's inner wall. The tetrodes were connected to a tethered head stage that included two LEDs
472 (1 red and one infra-red, 4 cm apart) for optical tracking (Cineplex 3, Plexon Inc.). Broadband neuronal
473 data were acquired at 22 kHz using a MAP system (Plexon Inc., Rasputin V2 software) and stored for
474 offline analysis. Spike sorting was performed manually based on trough and peak spike amplitude and

475 principal component analysis, using a custom Matlab script. Data was stored on a custom database
476 programmed using Datajoint (Yatsenko et al. 2015).

477 *Data analysis*

478 We used optical head tracking data to compute the following variables, which were divided into bins to
479 fit the LN model: (1) Allocentric position of the head (AP) in 2D, which ranged from -25 to 25cm in each
480 dimension, and was binned using a 12x12 grid. Note that AP is always included in a 25cm radius circle,
481 since the arena was circular, and therefore the corners of the 12x12 were never covered. However, the
482 LN model is designed in such a way that adding 'empty bins' won't affect its results. (2) Egocentric
483 position of the arena boundary (EB) was encoded in 2D, as described in **Suppl. Fig. 1**. Similar to AP, EB
484 ranged from -25 to 25cm, is always included in a 25cm radius circle, and was binned using a grid defined
485 in **Suppl. Fig. 1**. (3) Head direction (HD), which ranged from -180 to 180°. A HD of 0° corresponds to the
486 direction of the center of the black cue card. HD was divided in 18 bins. (4) Linear speed (LS) which
487 ranged from 0 to 30cm/s and was divided in 18 bins. (5) Angular speed (AS) which ranged from -150 to
488 150°/s and was divided in 18 bins. (6) Phase of the theta-band LFP (Θ P) was computed by applying a
489 Hilbert transform to band-pass filtered (5-12Hz) LFP signals, as in Hardcastle et al. 2017. Θ P ranged from
490 0 to 360° and was divided in 18 bins.

491 We used the same forward search procedure as in Hardcastle et al. (2015) to chose the best fitting
492 model.

493 Additional variables were tested but were excluded from the analysis after we determined that they
494 didn't contribute meaningfully to neuronal responses. We tested: (1) the egocentric direction of the
495 center of the cue card; (2) the point of the arena's boundary that the head faced, i.e. we computed the
496 intersection of the head's forward axis and of the arena boundary and divided the arena boundary in
497 bins, and (3) the frequency and (4) the magnitude of the LFP.

498 To ensure that results were robust, we excluded all recordings where AP covered less than 2/3 of the
499 bins included in the 25cm radius circle. We verified that this criterion was sufficient to ensure that all
500 other variables were well sampled. Two animals (H62M, H65M) were excluded from the analysis
501 because no session passed this criterion.

502 We computed the CV2 of the spike trains as the median value of $(2 \cdot |ISI_{i+1} - ISI_i| / (ISI_{i+1} + ISI_i))$ across all
503 inter-spike intervals (ISI).

504 *LN model fitting*

505 Model fitting was performed by using the Matlab code provided by the authors of (Hardcastle et al.
506 2017). We optimized the code to allow fitting a large number of models (up to 9 in preliminary testing).
507 We programmed it to fit only the models that were necessary for the forward search procedure. If n
508 variables are tested, this procedure will test, in a worst case, n 1st order models, n-1 2nd order models, n-
509 2 3rd order models, and so on until 1 nth order model; and the procedure will generally terminate earlier.
510 Therefore, fitting only these models instead of all possible models reduces the complexity from $2^n - 1$ in
511 all cases to $n \cdot (n+1) / 2$ in the worst case.

512 The LN model scores each model based on a log-likelihood measure. When a cell was recorded during
513 multiple sessions, the models were fitted to each session separately, and the resulting log-likelihood
514 averages across sessions.

515 Note that, when a model fits continuous firing rates as the LN model does (as opposed to firing rate
516 averaged across several trials), its coefficient of correlation will be heavily affected by the neuron's firing
517 variability, especially in the case of sparsely firing neurons such as hippocampal place cells. Since the
518 LN's model statistical analyses are based on log-likelihood, and comparing coefficients of correlation
519 across cell types and areas would easily be misleading, we opted not to report coefficients of
520 correlation.

521 *Shuffling test for HD and AP tuning*

522 We also quantified HD tuning by computing the mean vector length $|R|$ of the experimental HD tuning
523 curve. HD tuning curves were computed as a histogram $FR(HD)$ with a bin width of 20° and smoothed
524 using a Gaussian kernel (standard deviation 15°). $|R|$ was computed as $|R| = R = c \cdot \sum FR(HD) \cdot \exp(-i \cdot HD) /$
525 $\sum FR(HD)$ with $c = 3.6 \cdot \pi / 180 / 2 / \sin(1.8)$ (Zar, 1998).

526 We quantified AP tuning of the experimental AP tuning curve by computing the spatial information SI.
527 We divided the area in pixels (2.5cm width, Bjerknes et al. 2018) as computed $SI = \sum p_i \cdot FR_i / FR_{avg} \cdot \log_2($
528 $FR_i / FR_{avg})$, where FR_i is the firing rate in the i^{th} pixel, FR_{avg} the average firing rate, and p_i the probability of
529 being in the i^{th} pixel.

530 We implemented a shuffling test to assess the significance of $|R|$ and SI. For each cell, we generated
531 1000 samples by circularly shifting the spikes train by a random value of at least $\pm 10s$ (i.e. the shifted
532 trial was wrapped to the beginning) and we recomputed $|R|$ and SI. The un-shuffled values of $|R|$ and SI
533 were considered significant if they exceeded 99% of the shuffled values.

534 *Additional data from Peyrache et al. 2015, 2017*

535 In order to supplement our recordings in the ATN, we analyzed published recordings (Peyrache et al.
536 2015, 2017) performed in the ATN of 6 mice (named AP12, AP17, AP20, AP24, AP25, AP28, AP32 here,
537 corresponding to Mouse12, Mouse17, etc in the original dataset), as well as in the post-subiculum of 3
538 mice (AP24, AP25, AP28) while animals walked freely in a rectangular arena (53x46 cm). We included a
539 total of 39 sessions where animals covered the arena uniformly. We selected the shanks in which most
540 neurons were recorded, which likely correspond to the antero-dorsal nuclei and their immediate
541 vicinity, for population analysis (see **Suppl. Fig. 4,5**).

542 *Statistics*

543 We used a threshold value of 0.01 in all statistical tests. All statistical tests used in this study are non-
544 parametric. All comparisons between median values are performed using double-tailed Wilcoxon rank
545 tests.

546 *Data availability*

547 We provide a Supplementary Data spreadsheet as supplementary information. This spreadsheet
548 contains the response statistics of all cells shown in Figs. 6,7,8 and Suppls. Fig. 2,3,4,6,8,9,10,12,13,14.

549 *Code availability*

550 Data was analyzed based on code provided by the authors of (Hardcastle et al. 2017). Code used
551 specifically in this study will be made available upon request.

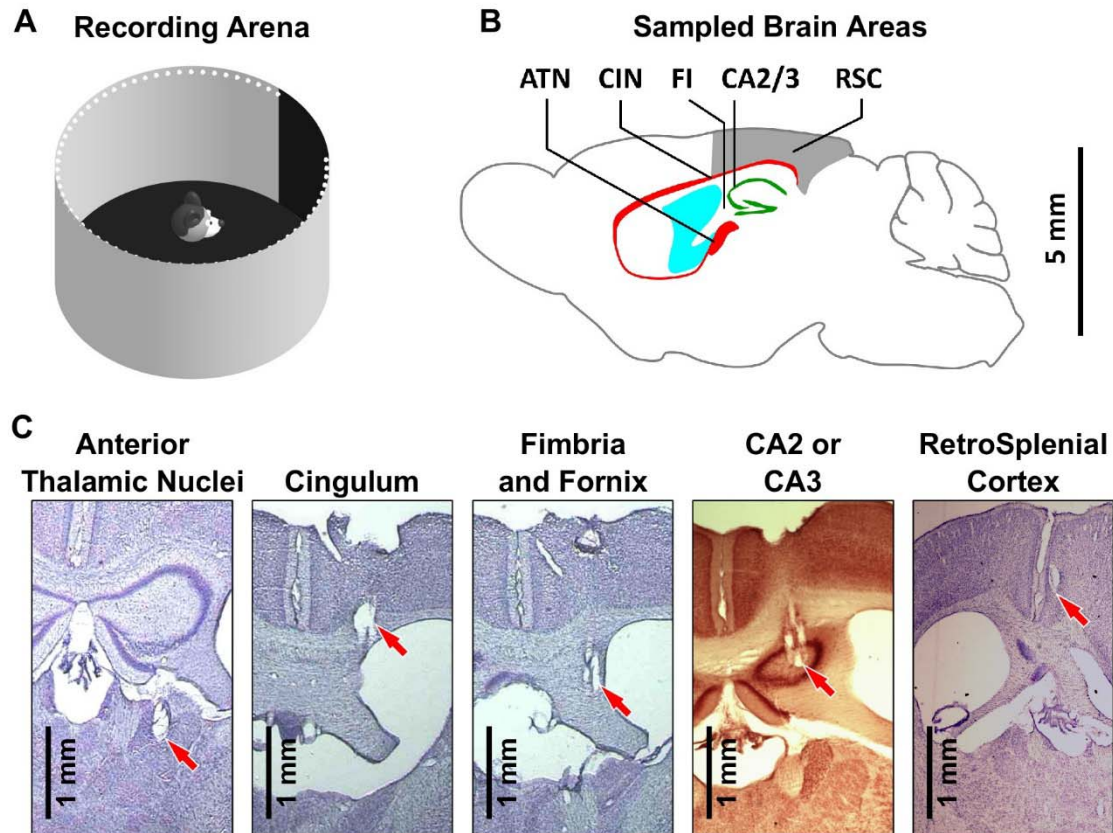
References

- 553
554
555 1. Adelmann, G., Deller, T., & Frotscher, M. (1996). Organization of identified fiber tracts in the rat
556 fimbria-fornix: an anterograde tracing and electron microscopic study. *Anatomy and embryology*,
557 193(5), 481-493.
- 558 2. Albo, Z., Di Prisco, G. V., & Vertes, R. (2003). Anterior thalamic unit discharge profiles and coherence
559 with hippocampal theta rhythm. *Thalamus & Related Systems*, 2(2), 133-144.
- 560 3. Alexander, A., Carstensen, L., Hinman, J., Raudies, F., Chapman, G. W., & Hasselmo, M. (2019).
561 Egocentric boundary vector tuning of the retrosplenial cortex. *bioRxiv*, 702712.
- 562 4. Barry, J. M. (2015). Axonal activity in vivo: technical considerations and implications for the
563 exploration of neural circuits in freely moving animals. *Frontiers in neuroscience*, 9, 153.
- 564 5. Bjerknes, T. L., Dagslott, N. C., Moser, E. I., & Moser, M. B. (2018). Path integration in place cells of
565 developing rats. *Proceedings of the National Academy of Sciences*, 201719054.
- 566 6. Blair, H. T., & Sharp, P. E. (1996). Visual and vestibular influences on head-direction cells in the
567 anterior thalamus of the rat. *Behavioral neuroscience*, 110(4), 643.
- 568 7. Bubb, E. J., Metzler-Baddeley, C., & Aggleton, J. P. (2018). The cingulum bundle: Anatomy, function,
569 and dysfunction. *Neuroscience & Biobehavioral Reviews*.
- 570 8. Bubb, E. J., Kinnavane, L., & Aggleton, J. P. (2017). Hippocampal–diencephalic–cingulate networks
571 for memory and emotion: An anatomical guide. *Brain and neuroscience advances*, 1,
572 2398212817723443.
- 573 9. Buzsáki, G., & Moser, E. I. (2013). Memory, navigation and theta rhythm in the hippocampal-
574 entorhinal system. *Nature neuroscience*, 16(2), 130.
- 575 10. Cacucci, F., Lever, C., Wills, T. J., Burgess, N., & O'Keefe, J. (2004). Theta-modulated place-by-
576 direction cells in the hippocampal formation in the rat. *Journal of Neuroscience*, 24(38), 8265-8277.
- 577 11. Clark, B. J., Simmons, C. M., Berkowitz, L. E., & Wilber, A. A. (2018). The retrosplenial-parietal
578 network and reference frame coordination for spatial navigation. *Behavioral neuroscience*, 132(5),
579 416.
- 580 12. Chen, L. L., Lin, L. H., Green, E. J., Barnes, C. A., & McNaughton, B. L. (1994a). Head-direction cells in
581 the rat posterior cortex. *Experimental Brain Research*, 101(1), 8-23.
- 582 13. Chen, L. L., Lin, L. H., Barnes, C. A., & McNaughton, B. L. (1994b). Head-direction cells in the rat
583 posterior cortex. II. Contributions of visual and ideothetic information to the directional firing.
584 *Experimental brain research*, 101(1), 24-34.
- 585 14. Cho, J., & Sharp, P. E. (2001). Head direction, place, and movement correlates for cells in the rat
586 retrosplenial cortex. *Behavioral neuroscience*, 115(1), 3.
- 587 15. Derdikman, D. (2009). Are the boundary-related cells in the subiculum boundary-vector cells?.
588 *Journal of Neuroscience*, 29(43), 13429-13431.
- 589 16. Finkelstein, A., Derdikman, D., Rubin, A., Foerster, J. N., Las, L., & Ulanovsky, N. (2015). Three-
590 dimensional head-direction coding in the bat brain. *Nature*, 517(7533), 159.

- 591 17. Gofman, X., Tocker, G., Weiss, S., Boccara, C. N., Lu, L., Moser, M. B., ... & Derdikman, D. (2019).
592 Dissociation between Postrhinal Cortex and Downstream Parahippocampal Regions in the
593 Representation of Egocentric Boundaries. *Current Biology*.
- 594 18. Góis, Z. H. T., & Tort, A. B. (2018). Characterizing Speed Cells in the Rat Hippocampus. *Cell reports*,
595 25(7), 1872-1884.
- 596 19. Hardcastle, K., Maheswaranathan, N., Ganguli, S., & Giocomo, L. M. (2017). A multiplexed,
597 heterogeneous, and adaptive code for navigation in medial entorhinal cortex. *Neuron*, 94(2), 375-
598 387.
- 599 20. Hinman, J. R., Chapman, G. W., & Hasselmo, M. E. (2019) Neuronal representation of environmental
600 boundaries in egocentric coordinates. *Nature Communications*, 10.
- 601 21. Jacob, P. Y., Casali, G., Spieser, L., Page, H., Overington, D., & Jeffery, K. (2017). An independent,
602 landmark-dominated head-direction signal in dysgranular retrosplenial cortex. *Nature neuroscience*,
603 20(2), 173.
- 604 22. Jeantet, Y., & Cho, Y. H. (2012). Evolution of hippocampal spatial representation over time in mice.
605 *Neurobiology of learning and memory*, 98(4), 354-360.
- 606 23. Kinsky, N. R., Sullivan, D. W., Mau, W., Hasselmo, M. E., & Eichenbaum, H. B. (2018). Hippocampal
607 place fields maintain a coherent and flexible map across long timescales. *Current Biology*.
- 608 24. Kornienko, O., Latuske, P., Bassler, M., Kohler, L., & Allen, K. (2018). Non-rhythmic head-direction
609 cells in the parahippocampal region are not constrained by attractor network dynamics. *eLife*, 7,
610 e35949.
- 611 25. Lozano, Y. R., Page, H., Jacob, P. Y., Lomi, E., Street, J., & Jeffery, K. (2017). Retrosplenial and
612 postsubicular head direction cells compared during visual landmark discrimination. *Brain and
613 Neuroscience Advances*, 1, 2398212817721859.
- 614 26. Maris, E., Fries, P., & van Ede, F. (2016). Diverse phase relations among neuronal rhythms and their
615 potential function. *Trends in neurosciences*, 39(2), 86-99.
- 616 27. Mizumori, S. J., & Williams, J. D. (1993). Directionally selective mnemonic properties of neurons in
617 the lateral dorsal nucleus of the thalamus of rats. *Journal of Neuroscience*, 13(9), 4015-4028.
- 618 28. Muller, R. U., Bostock, E., Taube, J. S., & Kubie, J. L. (1994). On the directional firing properties of
619 hippocampal place cells. *Journal of Neuroscience*, 14(12), 7235-7251.
- 620 29. Muzzio, I. A., Levita, L., Kulkarni, J., Monaco, J., Kentros, C., Stead, M., ... & Kandel, E. R. (2009).
621 Attention enhances the retrieval and stability of visuospatial and olfactory representations in the
622 dorsal hippocampus. *PLoS biology*, 7(6), e1000140.
- 623 30. O'Keefe, J., & Dostrovsky, J. (1971). The hippocampus as a spatial map: Preliminary evidence from
624 unit activity in the freely-moving rat. *Brain research*.
- 625 31. O'Keefe, J. (1976). Place units in the hippocampus of the freely moving rat. *Experimental neurology*,
626 51(1), 78-109.
- 627 32. Page, H. J., Wilson, J. J., & Jeffery, K. J. (2017). A dual-axis rotation rule for updating the head
628 direction cell reference frame during movement in three dimensions. *Journal of neurophysiology*,
629 119(1), 192-208.

- 630 33. Peyrache, A., Lacroix, M. M., Petersen, P. C., & Buzsáki, G. (2015). Internally organized mechanisms
631 of the head direction sense. *Nature neuroscience*, *18*(4), 569.
- 632 34. Peyrache, A., Schieferstein, N., & Buzsáki, G. (2017). Transformation of the head-direction signal into
633 a spatial code. *Nature communications*, *8*(1), 1752.
- 634 35. Preston-Ferrer, P., Coletta, S., Frey, M., & Burgalossi, A. (2016). Anatomical organization of
635 presubicular head-direction circuits. *Elife*, *5*, e14592.
- 636 36. Robbins, A. A., Fox, S. E., Holmes, G. L., Scott, R. C., & Barry, J. M. (2013). Short duration waveforms
637 recorded extracellularly from freely moving rats are representative of axonal activity. *Frontiers in*
638 *neural circuits*, *7*, 181.
- 639 37. Rubin, A., Yartsev, M. M., & Ulanovsky, N. (2014). Encoding of head direction by hippocampal place
640 cells in bats. *Journal of Neuroscience*, *34*(3), 1067-1080.
- 641 38. Skaggs, W. E., McNaughton, B. L., & Gothard, K. M. (1993). An information-theoretic approach to
642 deciphering the hippocampal code. In *Advances in neural information processing systems* (pp. 1030-
643 1037).
- 644 39. Simonnet, J., Nassar, M., Stella, F., Cohen, I., Mathon, B., Boccara, C. N., ... & Fricker, D. (2017).
645 Activity dependent feedback inhibition may maintain head direction signals in mouse presubiculum.
646 *Nature communications*, *8*, 16032.
- 647 40. Simonnet, J., & Fricker, D. (2018). Cellular components and circuitry of the presubiculum and its
648 functional role in the head direction system. *Cell and tissue research*, *373*(3), 541-556.
- 649 41. Taube, J. S. (1995). Head direction cells recorded in the anterior thalamic nuclei of freely moving
650 rats. *Journal of Neuroscience*, *15*(1), 70-86.
- 651 42. Tukker, J. J., Tang, Q., Burgalossi, A., & Brecht, M. (2015). Head-directional tuning and theta
652 modulation of anatomically identified neurons in the presubiculum. *Journal of Neuroscience*, *35*(46),
653 15391-15395.
- 654 43. Tsanov, M., Chah, E., Wright, N., Vann, S. D., Reilly, R., Erichsen, J. T., ... & O'Mara, S. M. (2010).
655 Oscillatory entrainment of thalamic neurons by theta rhythm in freely moving rats. *Journal of*
656 *neurophysiology*, *105*(1), 4-17.
- 657 44. Tsanov, M., Chah, E., Vann, S. D., Reilly, R. B., Erichsen, J. T., Aggleton, J. P., & O'Mara, S. M. (2011).
658 Theta-modulated head direction cells in the rat anterior thalamus. *Journal of Neuroscience*, *31*(26),
659 9489-9502.
- 660 45. Vann, S. D., & Aggleton, J. P. (2004). The mammillary bodies: two memory systems in one?. *Nature*
661 *Reviews Neuroscience*, *5*(1), 35.
- 662 46. Vertes, R. P., Hoover, W. B., & Di Prisco, G. V. (2004). Theta rhythm of the hippocampus: subcortical
663 control and functional significance. *Behavioral and cognitive neuroscience reviews*, *3*(3), 173-200.
- 664 47. Wang, C., Chen, X., Lee, H., Deshmukh, S. S., Yoganarasimha, D., Savelli, F., & Knierim, J. J. (2018).
665 Egocentric coding of external items in the lateral entorhinal cortex. *Science*, *362*(6417), 945-949.
- 666 48. Yatsenko, D., Reimer, J., Ecker, A. S., Walker, E. Y., Sinz, F., Berens, P., ... & Tolias, A. S. (2015).
667 DataJoint: managing big scientific data using MATLAB or Python. *bioRxiv*, 031658.
- 668 49. Yoder, R. M., & Taube, J. S. (2009). Head direction cell activity in mice: robust directional signal
669 depends on intact otolith organs. *Journal of Neuroscience*, *29*(4), 1061-1076.

- 670 50. Zar, J. H. Biostatistical Analysis 4th edn (Prentice Hall, 1998), pp.592-615.
- 671 51. Zugaro, M. B., Tabuchi, E., Fouquier, C., Berthoz, A., & Wiener, S. I. (2001). Active locomotion
672 increases peak firing rates of anterodorsal thalamic head direction cells. *Journal of Neurophysiology*,
673 86(2), 692-702.
- 674



675

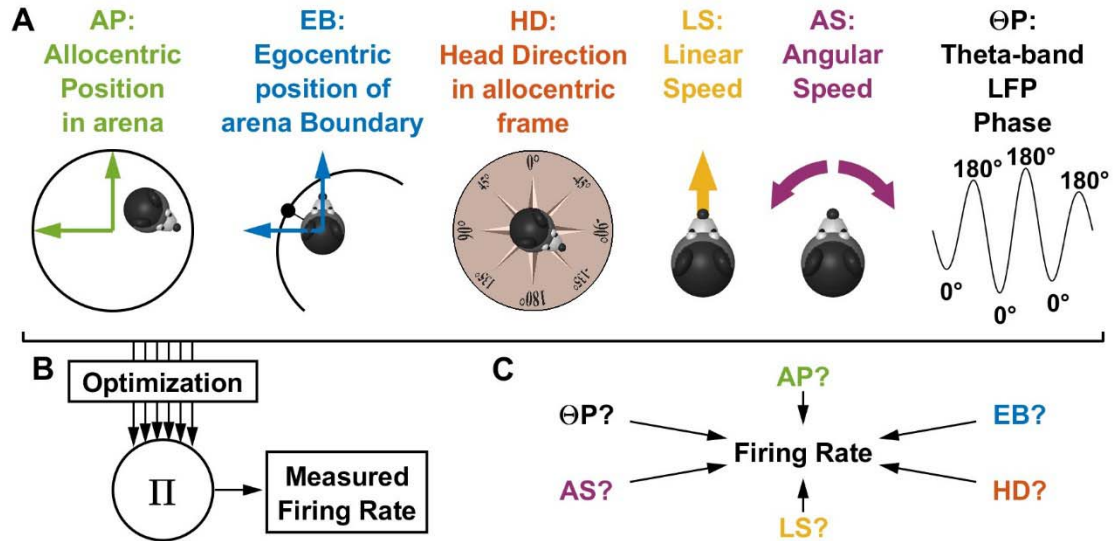
676 **Figure 1: Overview of the experimental approach.**

677 **A:** Experimental apparatus. Mice move freely in a circular arena (50 cm in diameter). A black card
678 provides an orienting cue.

679 **B:** Sagittal section of a mouse brain at ~ 1 mm lateral of the midline, with all recorded regions indicated.
680 ATN: Anterior Thalamic Nuclei. The cingulum fiber bundle (CIN) runs between the cortex and the corpus
681 callosum. The fimbria and fornix (FI) refer here to white matter regions located around the anterior
682 portion of the hippocampus. CA2/3: anterior portions of hippocampus. RSC: retrosplenial cortex.

683 **C:** Representative coronal sections showing tetraode track marks (red arrows) in all recorded areas (see
684 also **Fig. 6-10S1**).

685



686

687

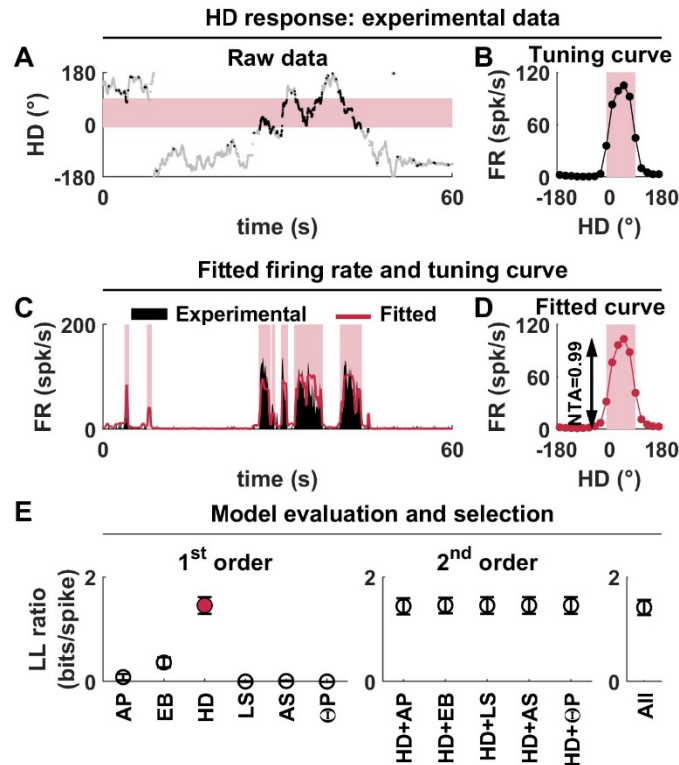
688 **Figure 2: Overview of the LN model (Hardcastle et al. 2017).**

689 **A:** Representation of the 6 variables used in the LN model. The color code is used in subsequent figures.

690 **B:** The model adjusts the tuning curve of all variables in order to fit the experimentally measured firing
691 rate optimally, using a gradient ascent procedure, and assuming that the variables interact
692 multiplicatively.

693 **C:** A search procedure is used to determine which variables contribute significantly to the cell's
694 response (see Methods).

695



696

697 **Figure 3: Example HD cell recorded in the ATN.**

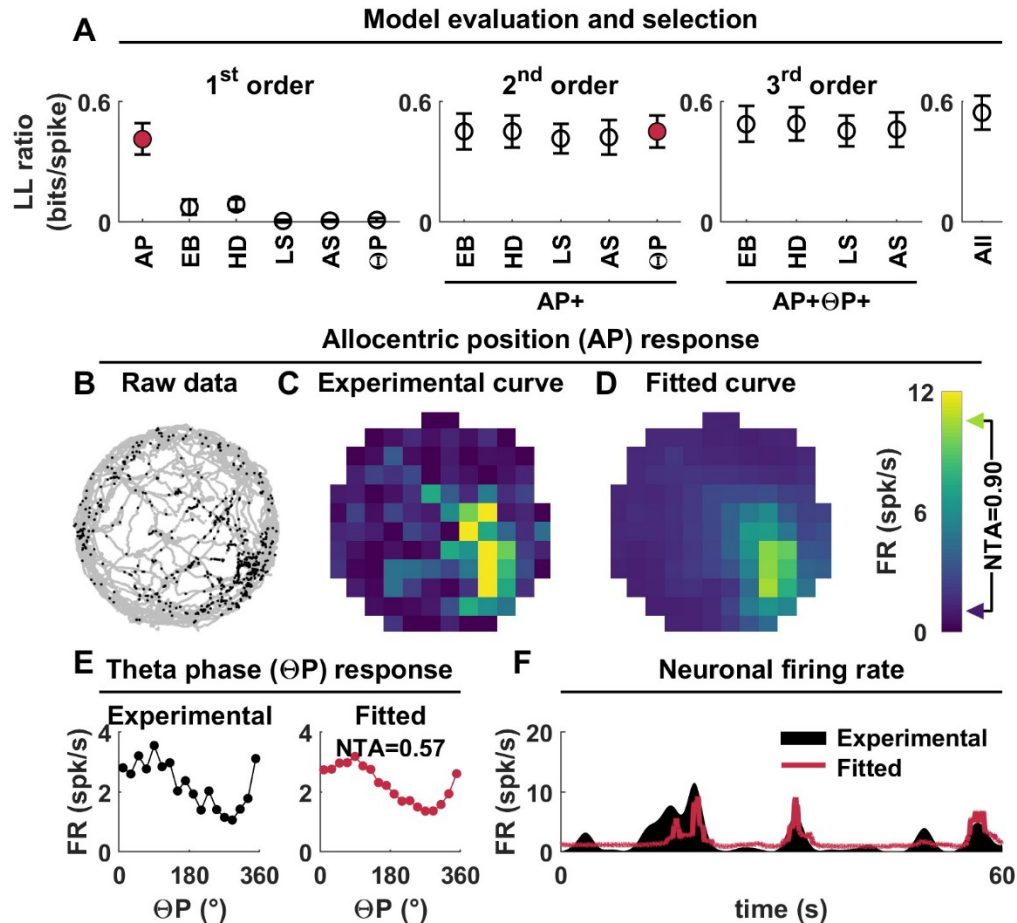
698 **A:** Raw data. The orientation of the animal as a function of time is shown in grey, and recorded spikes
 699 are overlaid as black dots. The cell fires preferentially when the animal's orientation is in the range of -
 700 10° to 90°, which is indicated by a pink band.

701 **B:** Traditional HD tuning curve computed by binning orientation data. The cell's preferred firing range is
 702 indicated in pink.

703 **C:** Model fit (red curve) to the cell's firing rate (black). Time periods where HD is within the preferred
 704 firing range are indicated in red. The cell fires consistently during these time periods, and this firing is
 705 accurately reproduced by the model.

706 **D:** HD tuning curve fitted by the LN model. In this simple example, the curve is identical to the
 707 experimental tuning curve in (B). Note, however, that this is not in general the case, as illustrated e.g. in
 708 Fig. 5E.

709 **E:** Illustration of the model selection procedure. Left panel: goodness of fit (LL ratio) of all 1st order
 710 models. The goodness of fit of the HD model is higher than any other model. Middle panel: goodness of
 711 fit of all 2nd order models. No model provides a significantly better fit than the HD model alone, which is
 712 therefore selected as the best model (red). Right panel: goodness of fit of the model including all
 713 variables, not significantly better than the HD model alone.



714

715 **Figure 4: Example place cell recorded in the hippocampus.**

716 **A:** Illustration of the model selection procedure. The LN model tested a set of 1st, 2nd and 3rd order
 717 models and selected the AP+ ΘP model (red). Therefore, this cell is modulated by the animal's allocentric
 718 position (AP) and tends to fire in phase with theta-band LFP.

719 **B:** Raw data. AP recorded over time is shown in grey, and recorded spikes are overlaid as black dots.

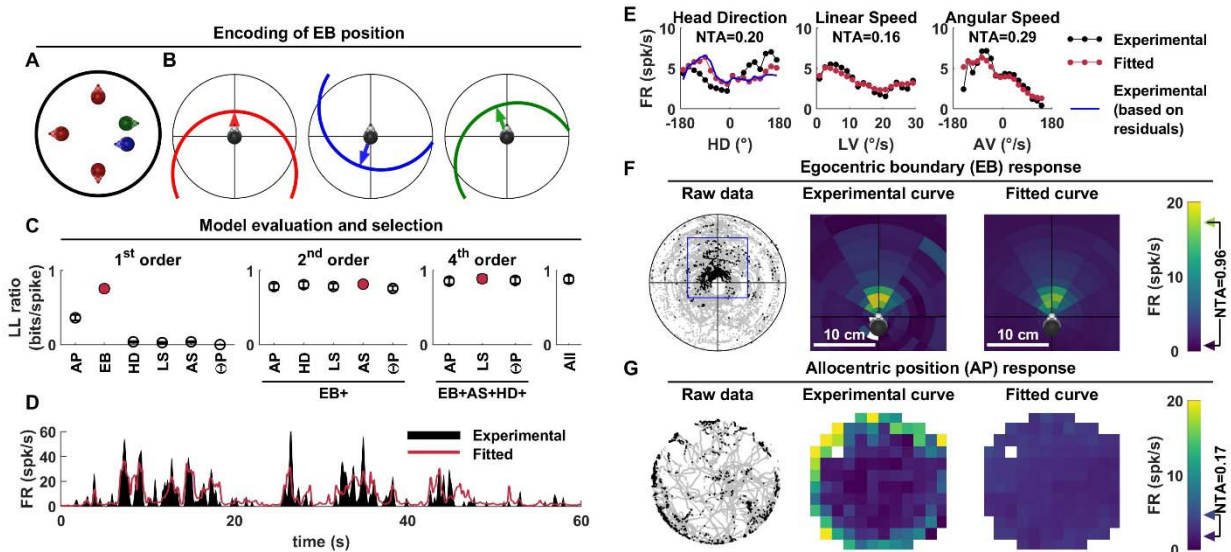
720 **C:** Experimental AP tuning curve computed in the traditional way by binning the data and represented as
 721 a color map (the color scale is shown to the right of panel D).

722 **D:** AP tuning curve fitted by the LN model. The curve resembles the experimental curve but is smoother
 723 due to the model's smoothness constraint.

724 **E:** Experimental (left) and fitted (right) ΘP tuning. The neuron responds preferentially at a phase of $\sim 90^{\circ}$,
 725 i.e. between the peak and the trough of the LFP.

726 **F:** Model fit (red curve) to a portion of the cell's firing rate (black).

727



728

729 **Figure 5: Example EBC recorded in RSC.**

730 **A:** Encoding of the egocentric position of the arena's boundary. Five possible positions of the head
 731 within the arena are shown. The 3 heads colored in red are placed 10 cm away from the boundary and
 732 facing directly towards it. Therefore, from an egocentric perspective, their position relative to the arena
 733 are identical, although their allocentric positions are different. The green and blue colored heads are
 734 placed at a similar position, but with different orientations relative to the arena boundary.

735 **B:** Egocentric positions corresponding to the allocentric positions for the example in A. Each panel
 736 corresponds to one example head position (or multiple equivalent positions for the first panel). The
 737 arena's boundary is drawn relative to the head, and an arrow points towards its closet point. Because
 738 the arena is circular, and its radius is known, the position of the entire boundary can be known on
 739 the position of the closet point of the boundary. Therefore, EB is represented as a 2D variable that
 740 encodes the position of the boundary closet point in egocentric coordinates (see **Suppl. Fig. 1** for
 741 details).

742 **C:** Illustration of the model selection procedure. A set of models is tested until the 4th order model
 743 EB+HD+AV+LS is selected as best fitting.

744 **D:** Model fit (red curve) to the cell's firing rate (black). The cell tends to fire in irregular bursts, some of
 745 which are not accurately predicted by the model, although the low-frequency response is consistently
 746 captured.

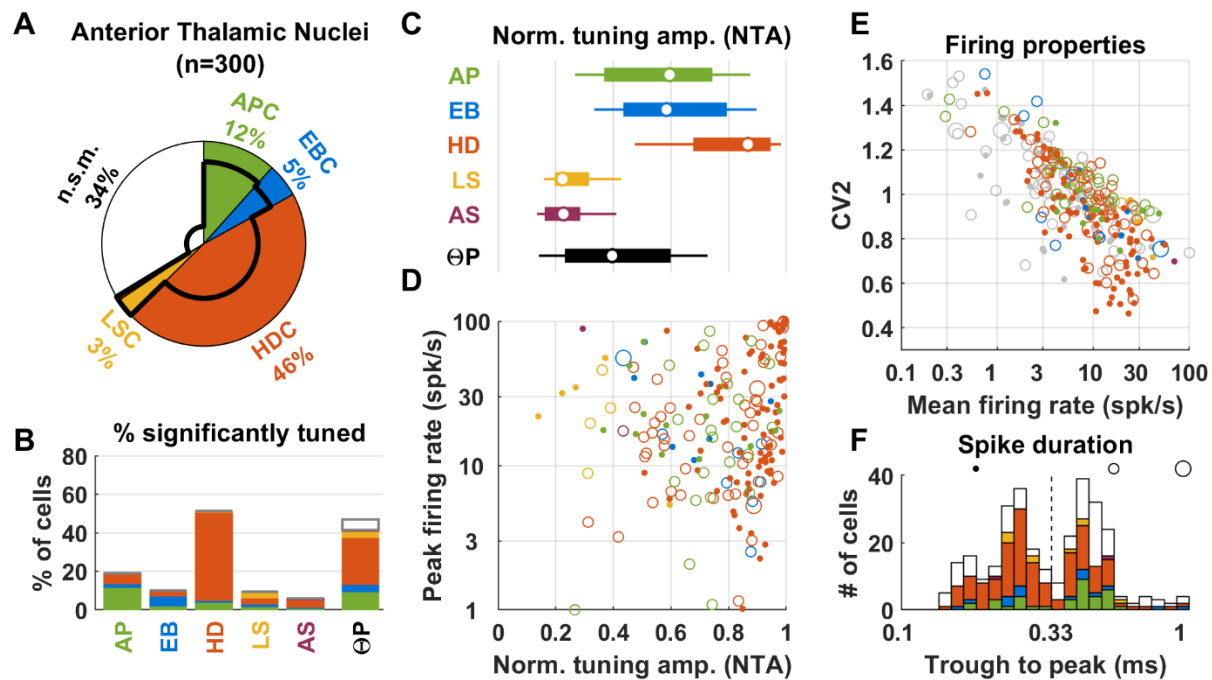
747 **E:** Experimental (black) and fitted (red) HD (left), LS (middle) and AS (right) tuning curves. The
 748 experimental HD tuning curve (black) does not correspond to the fitted tuning curve (red) because the
 749 former is heavily biased by the cell's sensitivity to EB. This can be demonstrated by fitting the EB model
 750 and re-computing the experimental HD tuning curve based on the residuals of that model. The resulting
 751 curve (blue) matches the fitted tuning curve closely.

752 **F:** Example cell's response to EB. Left: raw data, with EB encoded as shown in (B) and spikes overlaid as
753 black dots (see also **Suppl. Movie 1**). Middle: experimental tuning curve. Right: fitted tuning curve.

754 **G:** Example cell's response to AP. Same legend as in Fig. 4A-C. Although the cell appears tuned to AP
755 because it fires close to the boundary, its response is in fact a result of its EB tuning. The fitted curve is
756 flat, correctly reflecting the cell's absence of significant AP response.

757

758



759

760 **Figure 6: Population responses in the ATN. A:** Diagram of cell classification. The proportions of APC,
 761 ABC, HDC, LSC and ASC are shown by colored sectors. Non-spatially modulated (n.s.m.) cells are
 762 represented by the white sector. The proportion of Θ P-modulated cells in each sector is represented by
 763 a black line.

764 **B:** Proportion significant tuning to each variable, color-coded by cell classification based on its preferred
 765 stimulus. The white portion of the last bar represents the proportion of Θ P-modulated cells non-
 766 responsive to any other variable.

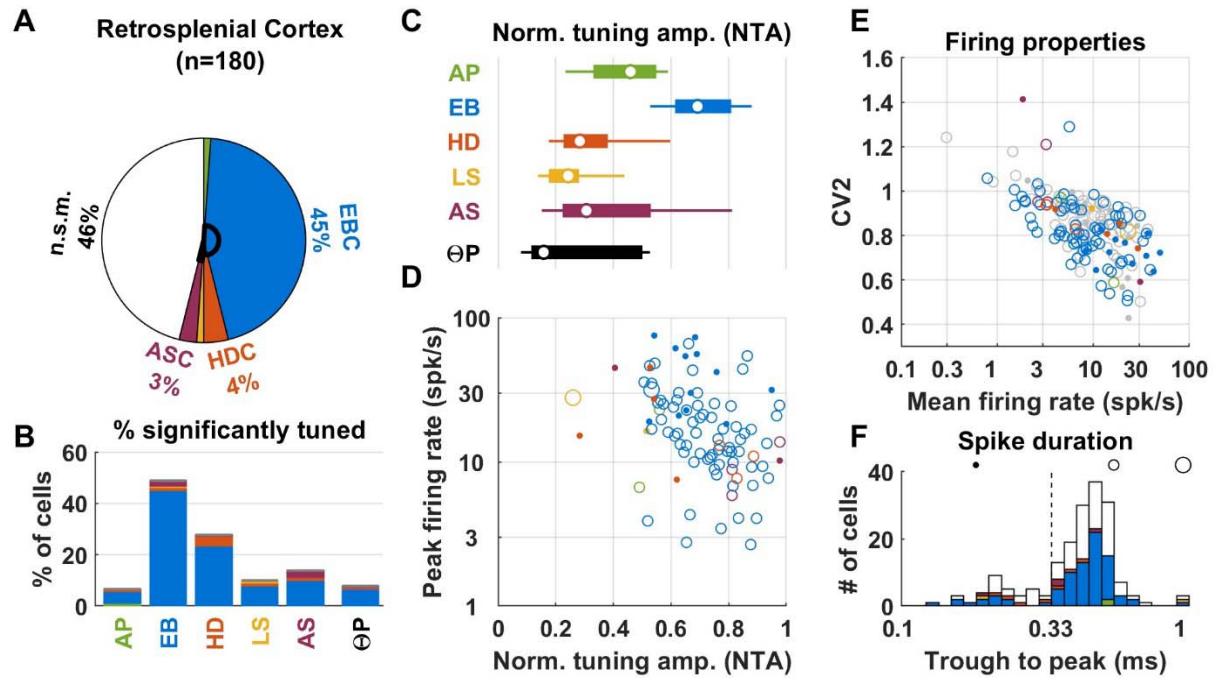
767 **C:** Normalized response amplitude (NRA) of AP, EB, HD, LS, AS and Θ P modulation. Circles/bars/whiskers
 768 represent the median, upper/lower quartiles and upper/lower deciles.

769 **D:** Peak firing rate versus NRA of all spatially-tuned cells (see panels A for color code). The size of the
 770 symbols encodes the trough to peak spike duration (small symbols: less than 0.33ms; medium symbols:
 771 between 0.33 and 0.8ms; large symbols: more than 0.8ms).

772 **E:** Firing properties (CV2 versus mean firing rate), color-coded as in panel D. Not spatially modulated
 773 cells are shown in grey.

774 **F:** Distribution of trough to peak spike duration, color-coded by cell classification. The black circle/disks
 775 illustrate the symbol size code used in panels D,E.

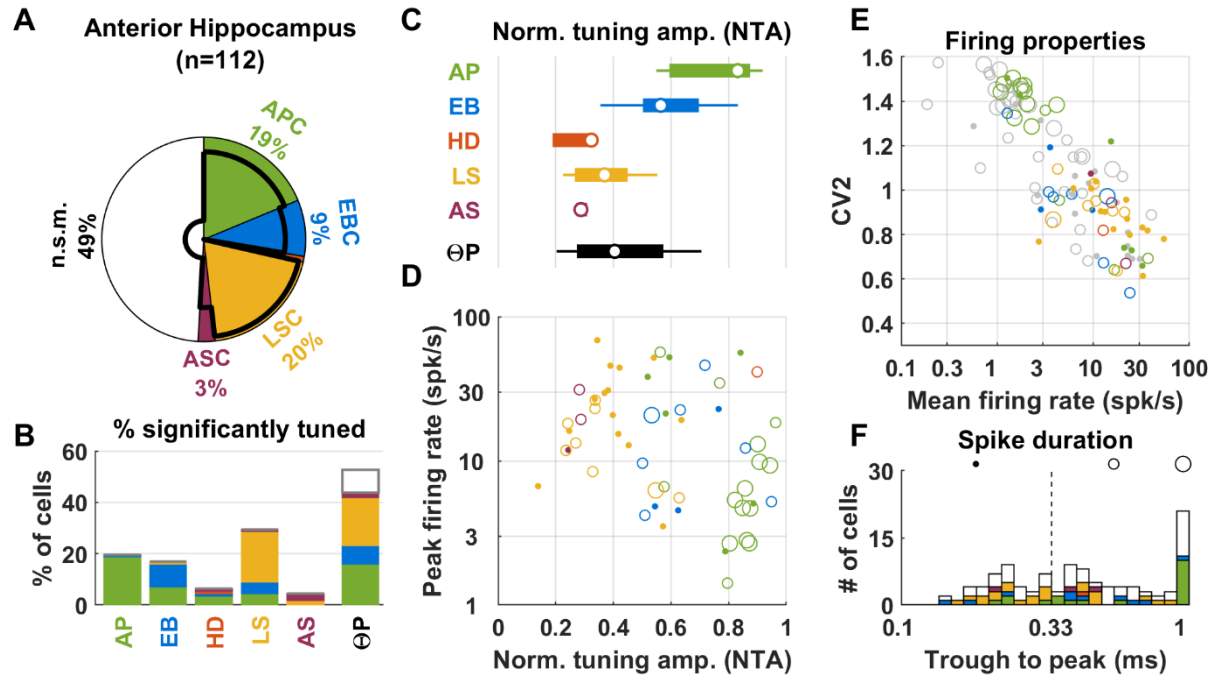
776



777

778 **Figure 7: Population response in the RSC. Same legend as in Fig. 6.**

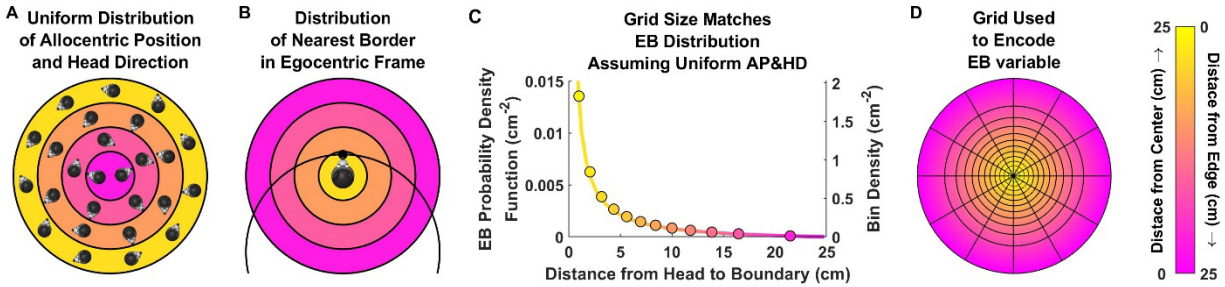
779



780

781 **Figure 8: Population responses in the hippocampus.** Same legend as in Fig. 6.

782



783

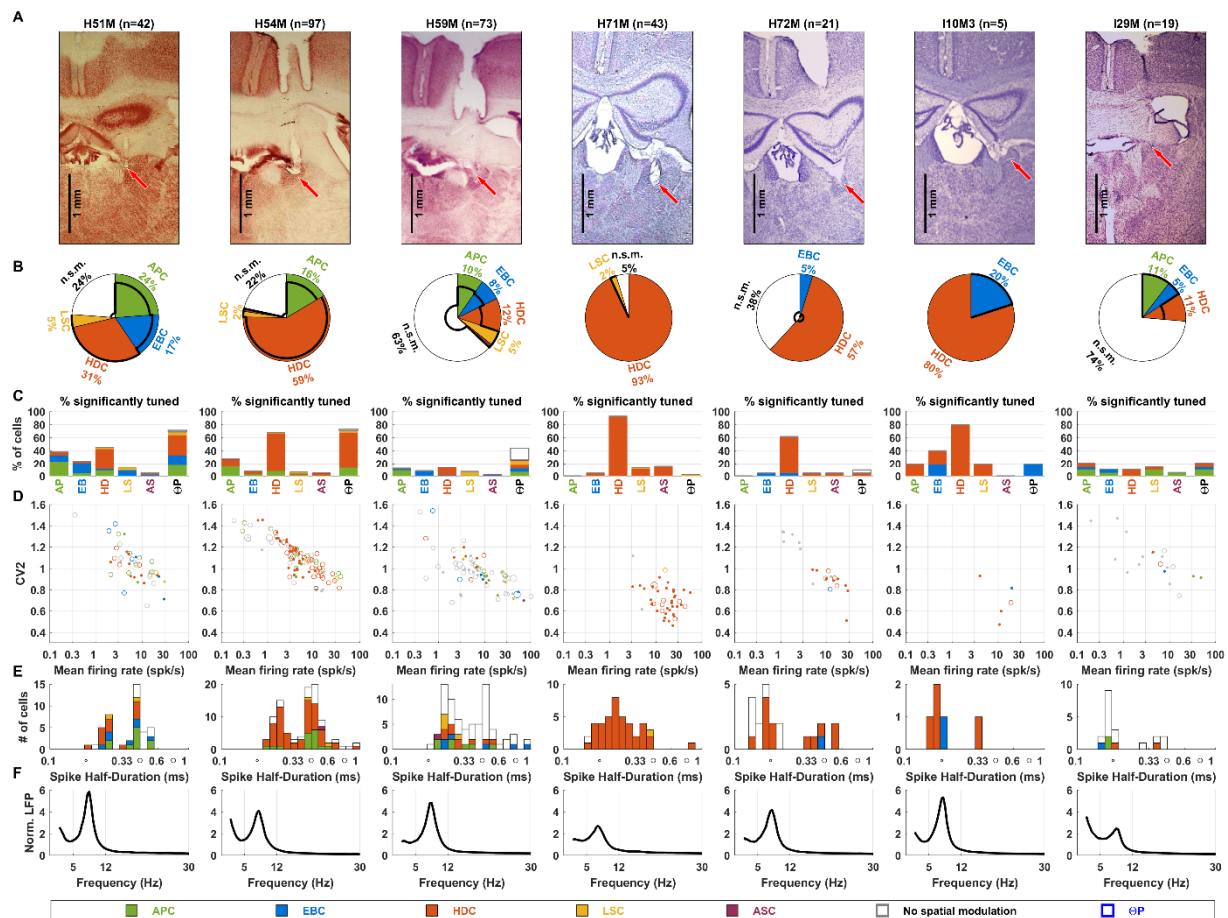
784 Supplemental Figure 1: Encoding the EB variable.

785 **A:** Arena seen from an allocentric point of view. The arena is divided in color-coded (yellow to magenta)
786 concentric regions. All regions have the same width; but outermost regions have a larger perimeter.
787 Therefore, the outer regions (e.g. yellow) have a larger surface area than the innermost (e.g. magenta).
788 If the animal explores the arena uniformly (as illustrated by the mice heads, where AP and HD are
789 uniformly distributed), the head is more likely to be located in the yellow regions.

790 **B:** In egocentric space, the egocentric position of the nearest boundary (EB) falls inside of a circle with
791 25 cm radius (since the closest boundary is at most 25 cm away from the head). Points where the head
792 is close to the boundary correspond to the (large) yellow region in A and to the (much smaller) yellow
793 region in B. Thus, if AP is uniformly distributed in A, EB is non-uniformly distributed in B, with a higher
794 probability of being close to the center.

795 **C:** Probability density function of EB (line), estimated by drawing a large (10^7) number of head positions
796 where AP and HD are uniformly distributed (as in panel A; we assumed that AP can't be located closer
797 than 0.5cm to the arena's wall to account for the animal's head size) and computing the corresponding
798 EB. The density function is expressed in probability per cm², and plotted here as a function of the
799 distance between the head and the boundary. The density is higher in proximal space (i.e. yellow
800 region). Accordingly, we bin the egocentric space in B with a grid that has a higher density (i.e. small
801 bins) in proximal space (dots, see panel D).

802 **D:** To represent EB, we created a grid that has a higher resolution in proximal space so as to match the
803 distribution in (C). First, we computed 12 concentric zones whose width was adjusted such that each
804 contained 1/12th of all samples used in C. Thus, by construction, EB is distributed uniformly across all
805 zones. All zones were further divided into 12 angular sectors to create a grid onto which EB is uniformly
806 distributed. The surface area of grid bins is computed and its inverse (grid density, in cm⁻²) is shown, as a
807 function of radius, in C. As expected, the resulting points (disks) scale with the EB density function.



808

809 **Supplemental Figure 2: Summary of ATN properties of individual mice.**

810 **A:** Coronal histology sections in each animal, showing the location of tetrode tracks. Tracks are
 811 predominantly located in the antero-dorsal nuclei, although they may possibly have contacted
 812 neighboring regions; e.g. antero-ventral nucleus in H71M; latero-dorsal nucleus in H72M; stria
 813 medullaris in H51M.

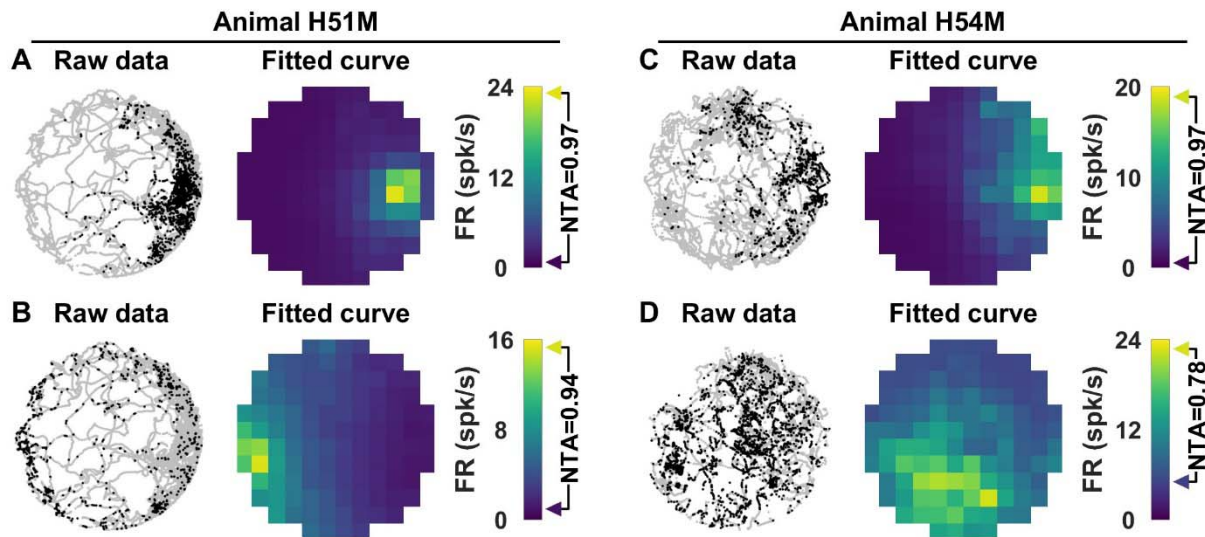
814 **B:** Venn diagram showing the proportions of all cell types and of Θ P-modulated cells, as in **Fig. 6A**. HDC
 815 were recorded in all animals. Clear populations (>5%) of APC and EBC were recorded in 3 and 4 animals
 816 respectively.

817 **C:** Proportion significant tuning to all variables, as in **Fig. 6B**.

818 **D:** Firing properties (CV2 versus mean firing rate) of recorded cells, as in **Fig. 6E**.

819 **E:** Distribution of trough to peak spike duration, as in **Fig. 6F**. **F:** Average (over all electrodes and
 820 recording sessions) LFP power spectrum. A clear theta-band LFP, peaking between 5 and 12Hz, was
 821 observed in all animals.

822

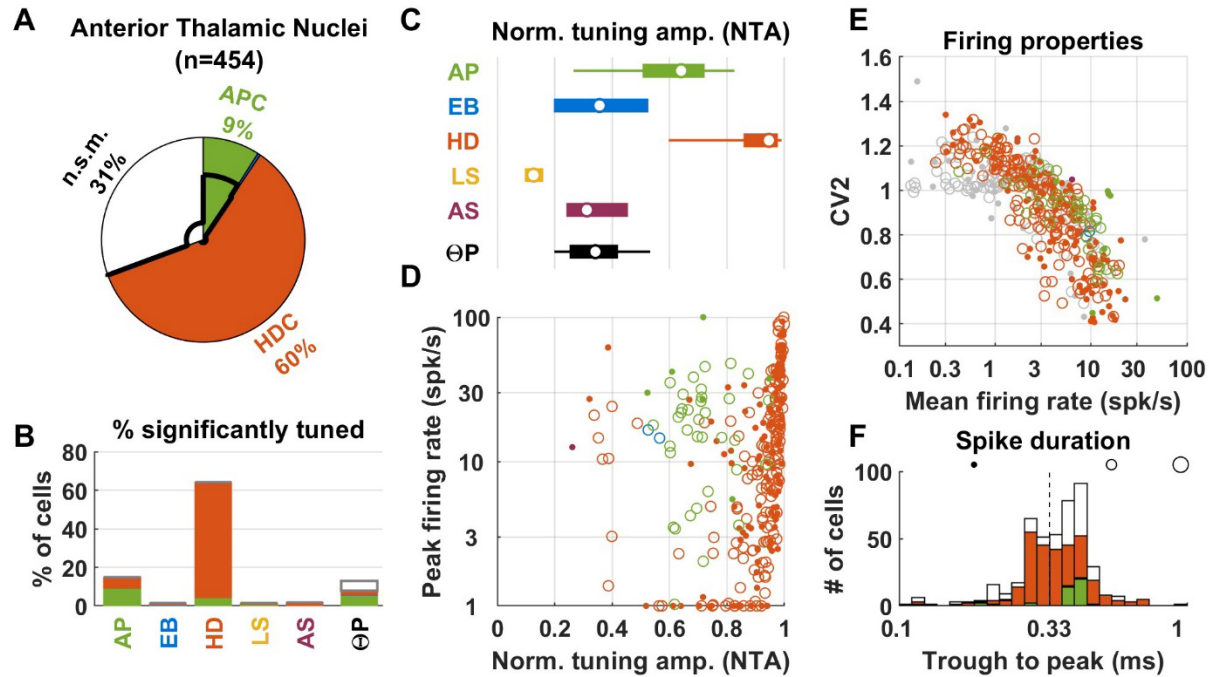


823

824 **Supplemental Figure 3: Example APC cells in the ATN.** Left panels: raw data, showing the recorded head
825 position (grey) and spikes overlaid as black dots. Right panels: fitted tuning curve represented as color
826 maps. The NTA is indicated on the color scale.

827

828



829

830 **Supplemental Figure 4: Population responses in the ATN from previously published data (Peyrache et**
 831 **al. 2015).** Same legend as in Fig. 6.

832 In agreement with our recordings, a large fraction (60%, panel A) of ATN cells are classified as HDC, with
 833 high NTA and peak firing (e.g. $NTA > 0.9$, peak firing > 30 spk/s), similar to our recordings. Across all
 834 significantly-tuned cells, HD responses have high NTA (panel C; median = 0.95; 1st – 9th decile: 0.6-0.99).

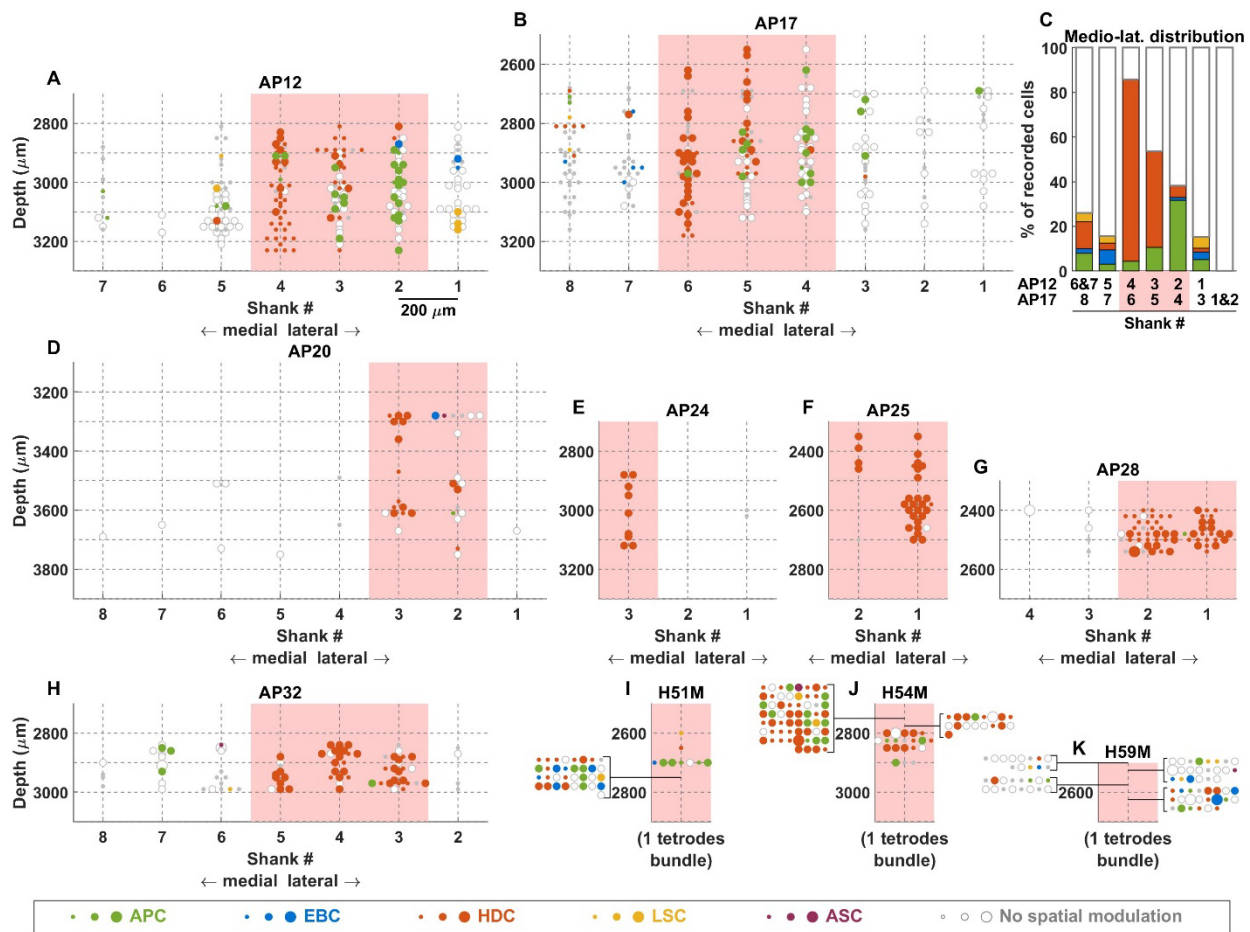
835 Note that HDC with very low peak firing (e.g. < 3 spk/s) amounted to a larger fraction of the population
 836 than in our recordings (23% vs. 3%; panel D). It is possible that longer recording durations used in
 837 Peyrache et al. 2015 (30 min foraging, total recordings amounting to several hours) made it easier to
 838 identify clusters of spikes occurring at low frequencies.

839 In agreement with our recordings, 9% of cells were classified as APC (panel A; see also **Suppl. Fig. 5**);
 840 median NTA = 0.64; 1st – 9th decile: 0.27-0.83; current study: = 0.63; 1st – 9th decile: 0.26-0.88; Wilcoxon
 841 rank sum test: $p=0.99$). Likewise, the distribution of APC's peak firing rates (median = 20 spk/s; 1st – 9th
 842 decile: 3.6-41) matched our recordings (median = 17 spk/s; 1st – 9th decile: 5-54; Wilcoxon rank sum test:
 843 $p=0.99$).

844 Similar to our recordings, we found a mixture of short-duration (39%) and long-duration (61%) spikes
 845 (panel F), although the bimodality was not as pronounced as in our data (compare with **Fig. 6F**) possibly
 846 because of differences in electrode type and filtering.

847

848



849

850 **Supplemental Figure 5: Spatial distribution of neuronal response types in ATN from previously**
 851 **published data (Peyrache et al. 2015) using multiple-shank probes (200 μm spacing between shanks).**

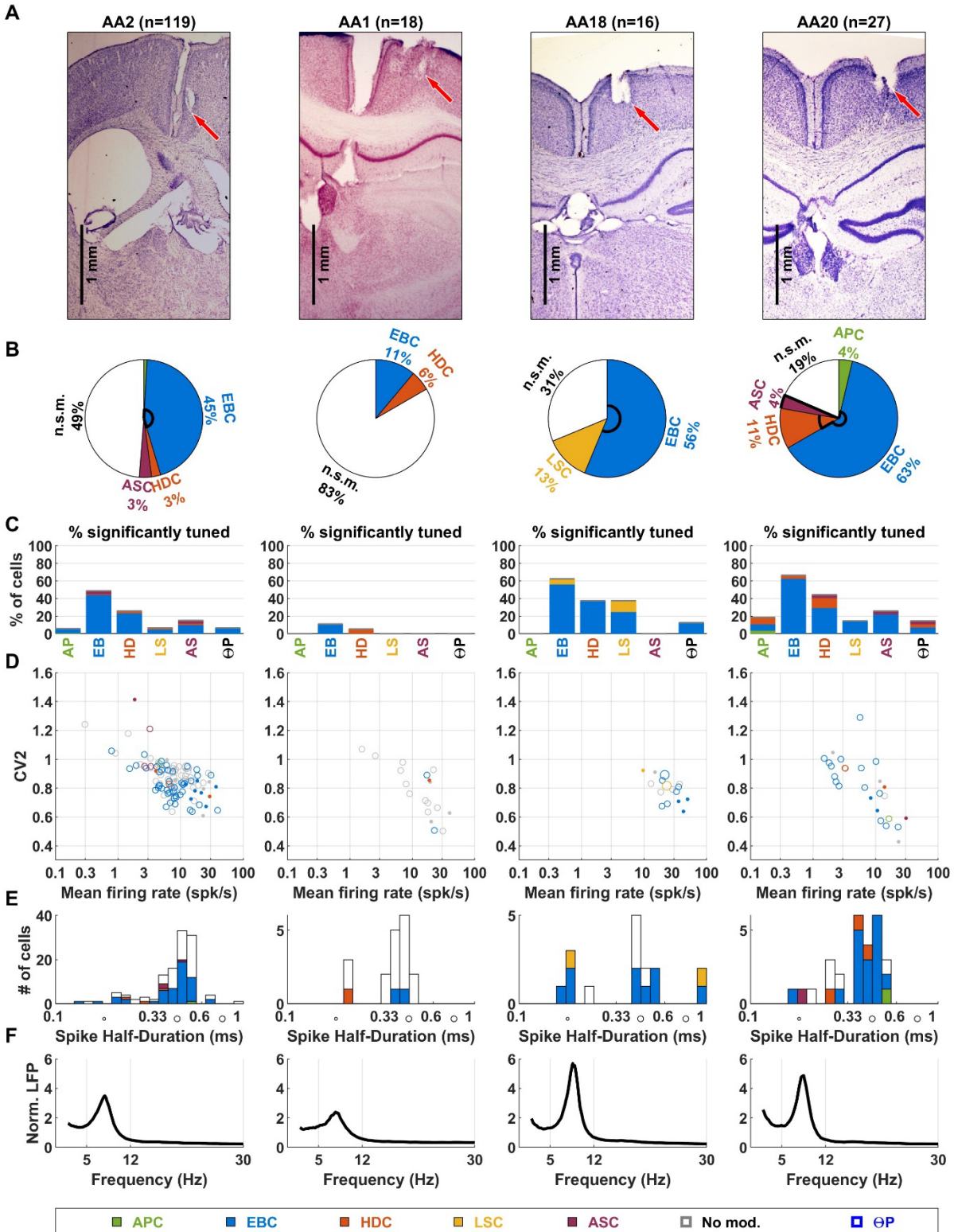
852 **A,B:** Cell location in animals AP12 and AP17, where most APC were found (abscissae: shank number,
 853 with shanks distributed along the medio-lateral axis; ordinate: depth relative to Bregma). Neurons
 854 recorded on a single shaft are staggered laterally for better visualization. Pink zone: region with most
 855 responsive neurons, likely the antero-dorsal nucleus and its immediate vicinity. Only neurons recorded
 856 in this region were included in the population analysis in **Suppl. Fig. 4**. HDC tend to cluster medially,
 857 APC laterally.

858 **C:** Percentage of cells of each classification as a function of medio-lateral position in animals AP12 and
 859 AP17, shifted to align the presumed location of ATN (pink). HDC were predominant (82% of recorded
 860 cells) in shanks #4 (AP12) and #6 (AP17) (leftmost bar), whereas APC were found more often in shanks
 861 #2 (AP12) and #4 (AP17) (32% of recorded cells). Thus, HDC and APC are spatially segregated in ATN,
 862 although with some overlap.

863 **D,H:** Location of neurons recorded in other animals by Peyrache et al. 2015.

864 **I,K:** Location of neurons in the present study (one tetrode bundle), for animals where APC were present
865 in the ATN intermingled with HDC. Large groups of cells recorded at a single location are represented at
866 the side of the graph for readability. We observe that HDC and APC are commonly recorded at a single
867 location. This indicates that these recordings were performed in a region where APC and HDC overlap.

868

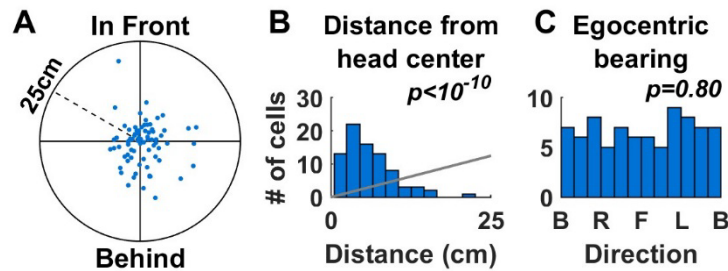


869

870 **Supplemental Figure 6: Recordings in the RSC of individual mice.** Same legend as in **Suppl. Fig. 2.**

871 Animal AA2 was implanted in the granular cortex, and AA1, AA18 and AA20 in the dysgranular cortex.

872



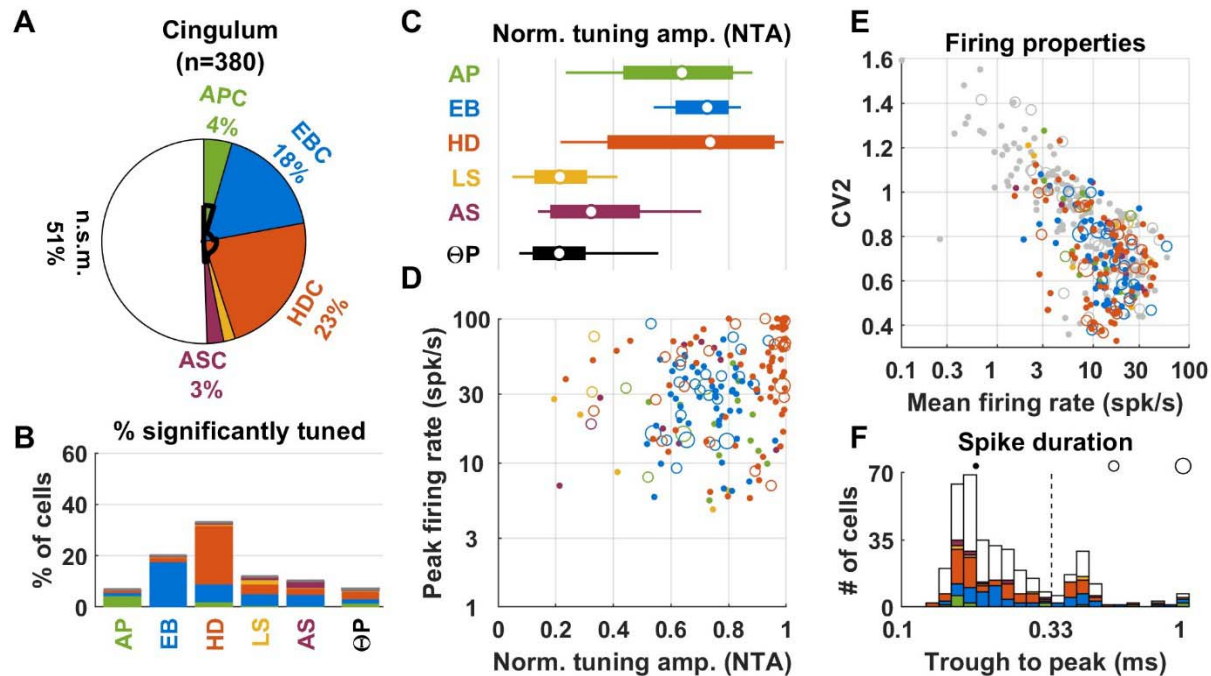
873

874 **Supplemental Figure 7: Spatial properties of EBC in RSC.**

875 **A:** Distribution of the preferred position of EBC. The preferred position refers to the egocentric location
876 of the nearest boundary (as in Fig. 2,5) at which the cell fires most, and is plotted in polar coordinates,
877 with the distance from the origin representing the distance from the head, and the direction
878 representing the egocentric bearing to the nearest point (i.e. in front of the head, to the right, behind
879 the head, or to the left).

880 **B:** Distribution of the distance from the head to the preferred position (histograms). Distribution
881 expected if points were distributed uniformly in panel A are shown in gray (H_0). P-values are computed
882 based on Kolmogorov-Smirnov test.

883 **C:** Distribution of the egocentric bearing to the preferred position. B, R, F, L refer to preferred position
884 occurring behind, right, in front or left of the head. P-values are computed based on circular Rayleigh
885 test for uniformity.



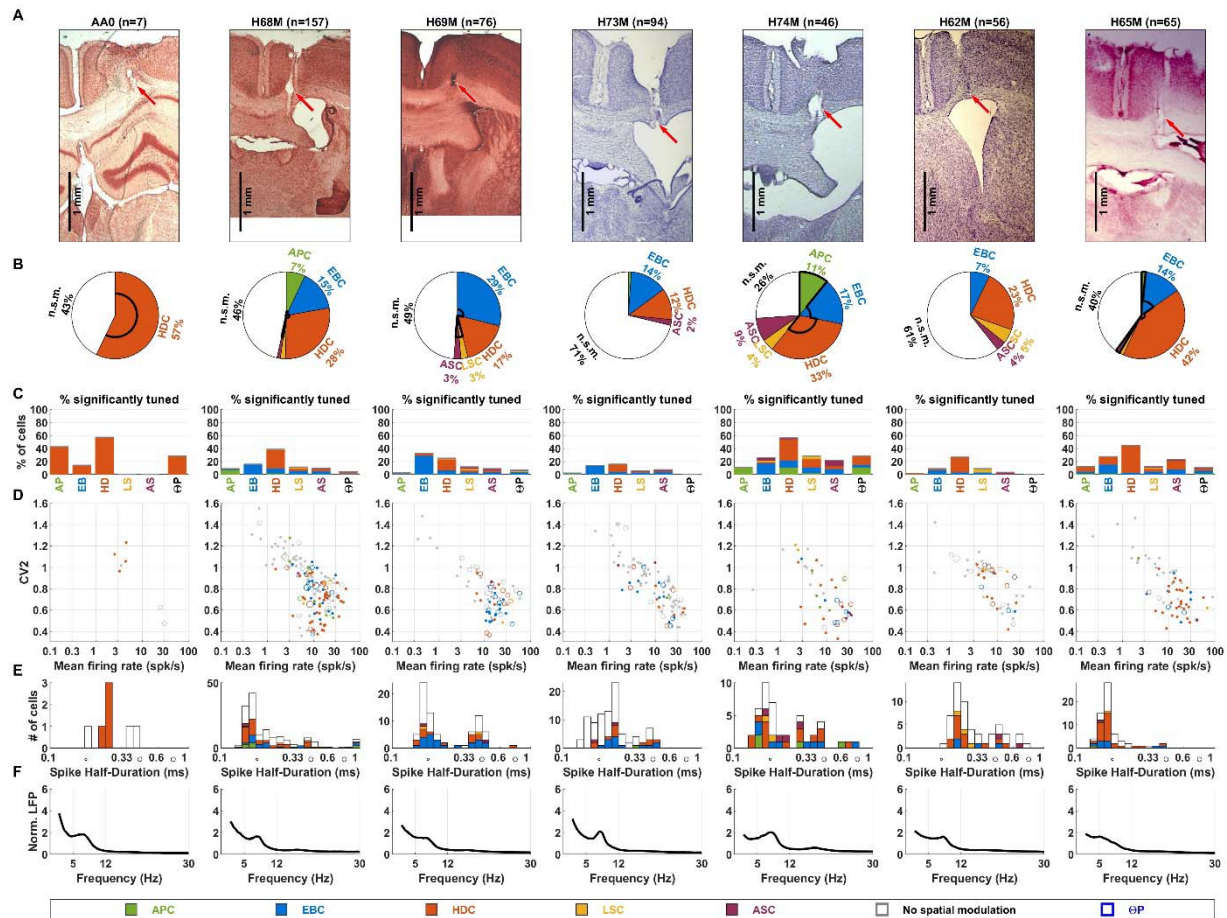
886

887 **Supplemental Figure 8: Population response in the cingulum.** Same legend as in Fig. 6. Summary data
 888 from 5 of 7 animals (Suppl. Fig. 9), excluding H62M and H65M (show in Suppl. Fig. 9) because of
 889 minimal locomotor behavior. Cingulum responses resembled a mixture of ATN and RSC neurons,
 890 consistent with anatomical studies showing that it conveys anterior thalamic and RSC projections (Bubb
 891 et al. 2018).

892 The majority of cells were classified as HDC (23%) or EBC (18%). For HD responses, the median NTA was
 893 0.92 (C), similar (Wilcoxon rank sum test, $p=0.16$) to ATN (0.89), with overlapping range (0.57-0.99 1st-9th
 894 decile). Because fewer neurons with low firing rate (e.g. ~ 3 spk/s or less) or low peak responses (e.g. ~ 10
 895 spk/s or less) were encountered (compare panels D,E with Fig. 6D,E), mean firing of HDC was
 896 significantly higher in the cingulum (mean firing: median = 14 vs 9 spk/s, $p=2.10^{-3}$, Wilcoxon rank sum
 897 test; peak firing: median = 48 vs 20 spk/s, $p<10^{-5}$).

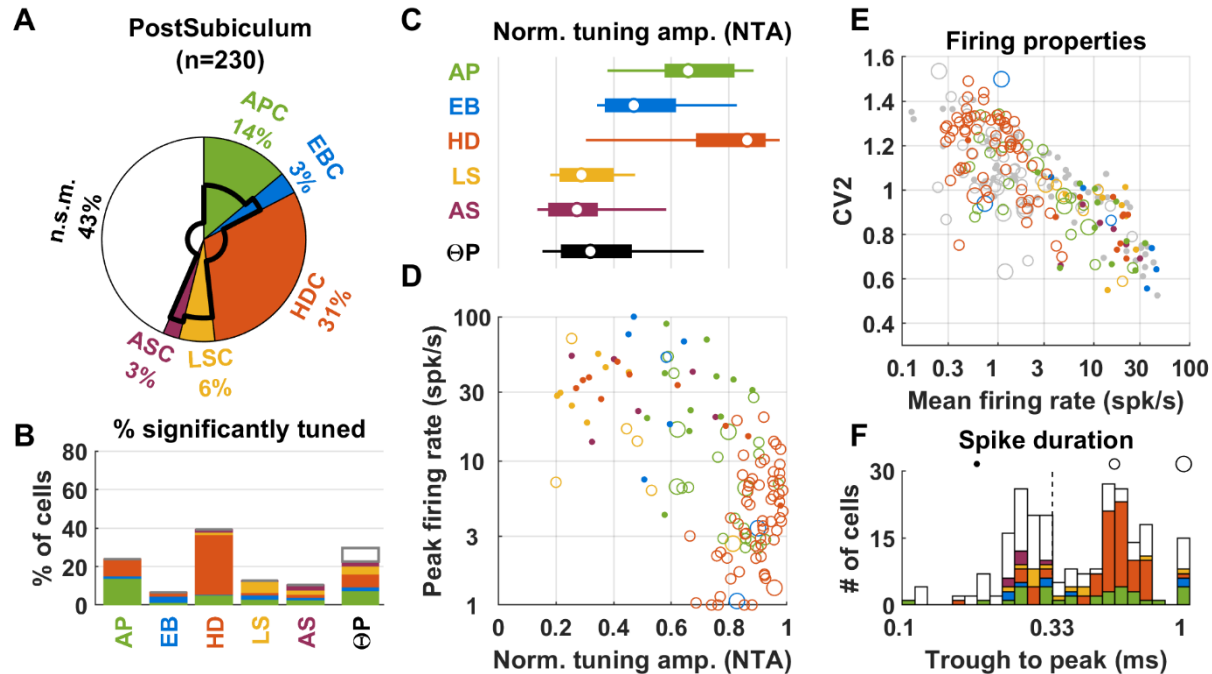
898 The NRA of EBC cells ranged from 0.57 to 0.84 (1st-9th decile, C), overlapping the distribution in RSC, with
 899 a similar median (0.75 vs. 0.7). Furthermore, 39% of cingulum EBC were also significantly tuned to HD,
 900 with median NRA=0.24 (B), in agreement with findings in RSC (Fig. 7B, $p=0.4$, Wilcoxon rank sum test).
 901 Cingulum EBC had larger firing rate (14 vs 8 spk/s, $p<2.10^{-3}$) and peak firing (30 vs 16 spk/s, $p<10^{-4}$)
 902 (compare panels D,E with Fig. 7D,E).

903 Small fractions of APC, LSC and ASC were encountered in the cingulum (A,B), with similar properties as in
 904 other regions. However, only a marginal theta rhythm could be identified in the LFP (see also Suppl. Fig.
 905 9). Accordingly, only a small fraction (7%) of neurons exhibited a significant ΘP modulation, and the
 906 amplitude of this modulation was very low (median: 0.21). The average firing rate and CV2 in the
 907 cingulum (E, Spearman rank correlation= -0.64 , $p<10^{-10}$) largely overlapped distributions in ATN and RSC.
 908 As expected, the majority of neurons (300/380, 79%) had short-duration spikes (F).



909

910 **Supplemental Figure 9: Recordings in the cingulum of individual mice.** Same legend as in **Suppl. Fig. 2.**
 911 Animals H62M and H65M exhibited minimal locomotor behavior and were excluded from the
 912 population analysis since criteria for coverage of the arena interior were never met (but included here as
 913 LN analysis is robust to partial arena coverage).



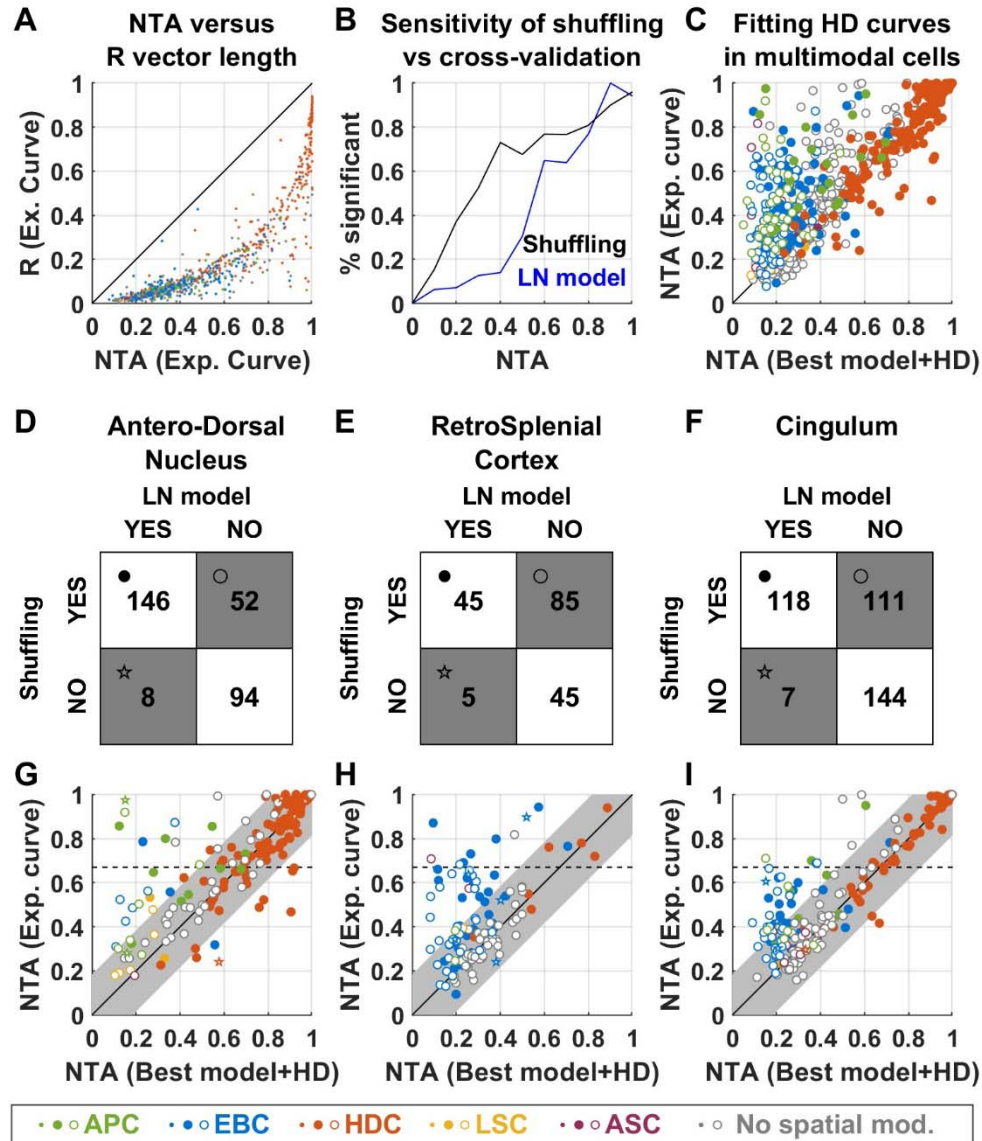
914

915 **Supplemental Figure 10: Population responses (3 animals, 230 neurons) in the Postsubiculum from**
 916 **previously published data (Peyrache et al. 2015). Same legend as in Fig. 6.**

917 The most prominent cell type (31%) was HDC (panel A,B). Most (61/71; 86%) HDC had long spike
 918 duration (panel F). These cells, which appear as large open orange symbols in panel D, had large NTA
 919 (median = 0.91; 1st-9th decile: 0.77-0.97) and low peak firing (median = 3.8 spk/s; 1st-9th decile: 1.2-10.5
 920 spk/s), likely correspond to layer 3 pyramidal neurons identified as the main population of postsubicular
 921 HDC in (Tukker et al. 2015, Preston-Ferrer et al. 2016, Simonnet et al, 2017; Simonnet et Fricker, 2017).

922 The second most prominent type (14%) was APC. Most (32/43, 74%) APC had long-duration spikes, and
 923 AP responses had generally large NTA (median = 0.67; 1st-9th decile: 0.38-0.89).

924 We noted that 12 APC were significantly tuned to HD and 20 HDC were significantly tuned to AP, such
 925 that, altogether, ~14% of the population encoded AP and HD conjunctively. Cells that encode these
 926 variables conjunctively were also reported by Caccuci et al. (2004), although most of these cells were Θ -
 927 modulated. In contrast, the conjunctive cells identified in our analysis of the Peyrache et al's (2015)
 928 dataset were rarely (9/32, 28%) Θ -modulated.



929

930 **Supplemental Figure 11: Classification of HD cells using the LN model versus traditional approaches.**

931 Here we analyze how the statistical approach used to classify HD cells in the LN model differs from
 932 traditional techniques where HD tuning is quantified by the mean vector length $|R|$, and statistical
 933 significance is evaluated by a shuffling test where $|R|$ is considered significant if it is larger than 99% of a
 934 set of $|R|$ values produced by randomly shifting the animal's motion relative to the neuronal spike train
 935 (Skaggs 1993; Finkelstein et al. 2015). Alternatively, many studies classify cells as HDC when $|R|$ exceeds
 936 a threshold, e.g. 0.26 (Jacobs et al. 2017) or 0.4 (Yoder and Taube 2009; Kornienko et al. 2018).

937 In contrast, the LN model tests for HD tuning by fitting a HD tuning curve to 90% of the recorded data
 938 and measuring how the fitted curve accounts for the cell's firing during the remaining 10%. This
 939 operation, called cross-validation, is repeated 10 times. A cell is considered HD tuned if the fitting
 940 quality is significantly larger than 0 (or than a previous model that doesn't include HD) based on a signed

941 rank test over these 10 samples. Another fundamental difference between the LN model and traditional
942 approaches is that the LN model fits the cell's firing with multiple variables simultaneously. Here, we
943 discuss how these differences affect the classification of HD cells by considering data from the ATN,
944 cingulum and RSC only (where most HD-tuned cells are found).

945 **A:** Comparison between the traditional measure, $|R|$, and the NTA measure used in this study. We
946 computed the $|R|$ and NTA values of the experimental tuning curves of all cells (regardless of whether
947 they were significantly tuned to HD). Most data points cluster tightly to form a curve, indicating that
948 there is a close (although non-linear) correspondence between $|R|$ and NTA. Cells are color-coded
949 based on the classification by the LN model (see legend).

950 **B:** Comparison between the sensitivities of the cross-validation and shuffling tests. We performed a
951 shuffling test on the $|R|$ value of all cells. Independently, we fitted a LN model where only HD was
952 included. Next, we computed the percentage of cells classified as HD-tuned based on a shuffling test
953 (black curve) or the LN model (blue curve) as a function of NTA. As expected, almost all cells pass both
954 tests when the NTA is high (>0.8). In contrast, fewer cells with intermediate NTA (0.2-0.8 range) pass the
955 LN model's cross-validation test. Thus, the cross-validation procedure is less sensitive than the shuffling
956 test.

957 **C:** Previous studies (Muller et al. 1994; Cacucci et al. 2004; Rubin et al. 2014) have pointed out that
958 responses to variables other than HD (e.g. AP or EB) can be erroneously interpreted as HD tuning. When
959 this happens, HD tuning will appear high when fitting the LN model with only the HD variable, or when
960 computing the experimental tuning curve, but will be lower when the response to other modalities is
961 accounted for, as done by the LN model in general. To appreciate this, we plot the NTA of the
962 experimental HD tuning curve versus the NTA of the HD curve fitted by the LN model. The latter was
963 computed based on the cell's best model (for HD-tuned cells) or by adding the HD variable to the best
964 model. Filled/open symbols represent HD tuned/not tuned based on the full LN model, color-coded
965 based on the classification by the LN model. Many AP and EB cells (green and blue) appear above the
966 diagonal, indicating that responses identified as AP or EB are erroneously interpreted as HD tuning when
967 considering only the HD model. This overestimation may happen in cells that are really HD tuned (closed
968 symbols) or not (open symbols).

969 From B and C, we conclude that (1) the shuffling test is more sensitive than the cross-validation
970 procedure, and that (2) computing NTA (or equivalently $|R|$) from experimental tuning curves is prone
971 to overestimating HD tuning in multimodal cells. Next, we examine how these approaches differ, in
972 practice, when applied to ATN, RSC and cingulum.

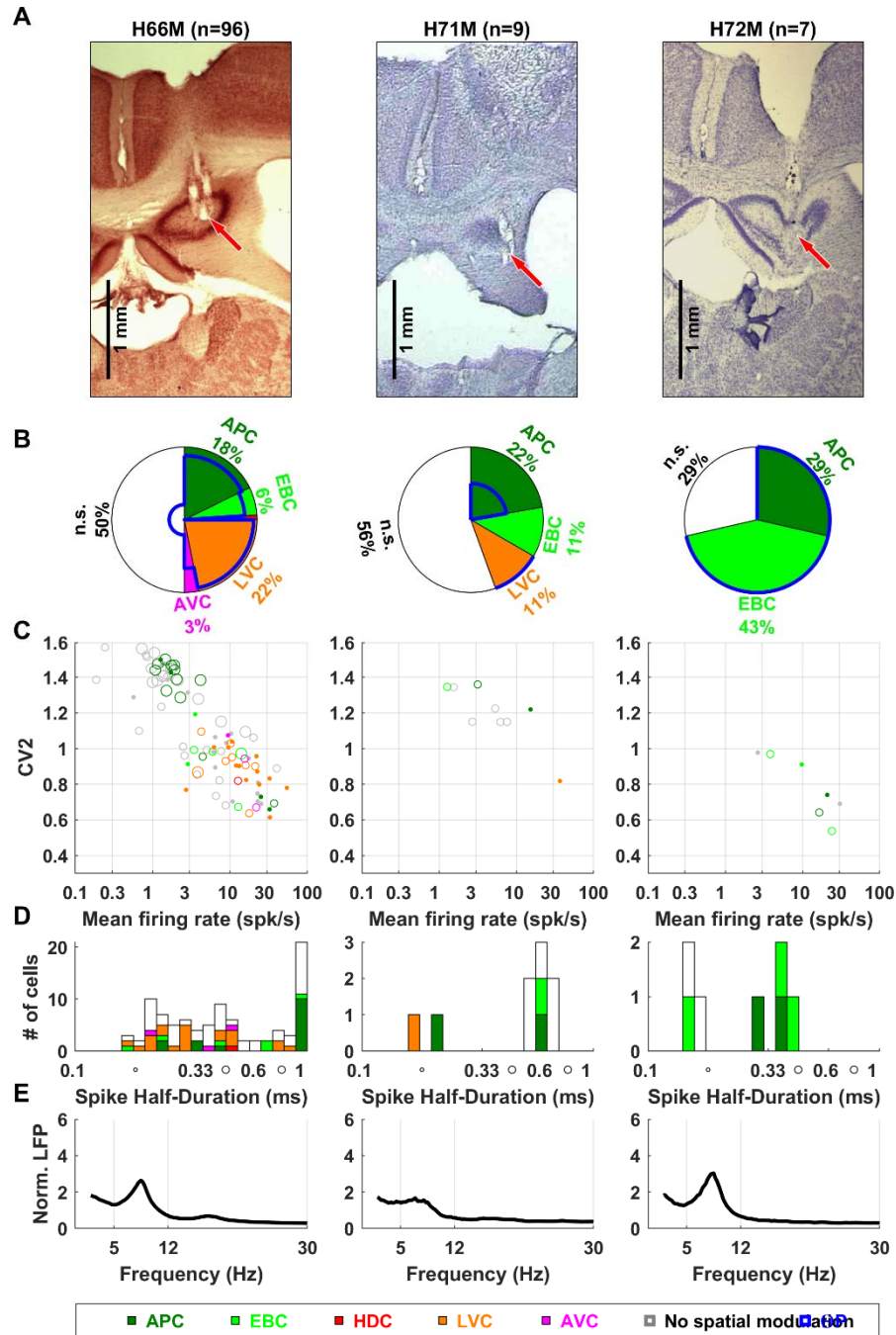
973 **D-F:** Contingency matrices indicating the number of cells classified as HD-tuned or not by the LN model
974 and shuffling method in ATN (D), RSC (E) and cingulum (F). The symbols shown in the matrix correspond
975 to the symbol code in panels G-I. The two methods generally agree in the ATN: 146 cells are classified as
976 HD-tuned and 94 as HD non-tuned by both, i.e. the classification matches in 240/300 (80%) cells. 52 cells
977 (17% of ATN) are classified as HD-tuned by only the shuffling method, and a negligible fraction by only

978 the LN model. The two classifications diverge to a larger extent in RSC and cingulum, where 48% and
979 27% of cells are classified as HD-tuned based on the shuffling methods only.

980 **G-I:** To elucidate the origin of these discrepancies, we plot the NTA of the experimental HD tuning curve
981 versus the curve fitted by the LN model (as in panel C). Cells that are HD-tuned based on both
982 classifications are shown as filled symbols. Cells that are HD-tuned based on the shuffling/cross-
983 validation methods only are shown as open disks/stars. Cells are color-coded based on the classification
984 by the LN model (see legend).

985 A sizeable fraction of cells are classified as HD tuned based on the shuffling method only (open symbols,
986 $n=248$ across all 3 areas), and we reason that this may occur for two reasons: (1) because the NTA of
987 some cells is overestimated when computing the experimental curve (see panel C), in which case cells
988 will appear above the diagonal and/or (2) because the shuffling test is more sensitive for cells with low
989 NTA (see panel B). To quantify approximately how many cells fall in each category, we estimate a
990 confidence interval around the diagonal by considering cells that are classified as HDC by both methods
991 (solid red). The confidence interval width is set at the 95% percentile of the distance distribution of
992 these cells from the diagonal (0.13). We find that 193/248 (78%) of open symbols fall within this
993 interval. These likely correspond to cells where HD tuning was likely *not* over-estimated, and that were
994 classified as HD-tuned because of the shuffling test's larger sensitivity. These cells are likely genuinely
995 HD-tuned, although with a low amplitude. In contrast, HD tuning may have been overestimated in cells
996 that appear above the interval (55/248; 22% of open symbols), and the classification as HD-tuned may
997 be erroneous. In total, this category of potentially mis-classified cells represents 16/300 (5%) ATN cells,
998 18/180 (10%) RSC cells and 19/380 (5%) cingulum cells.

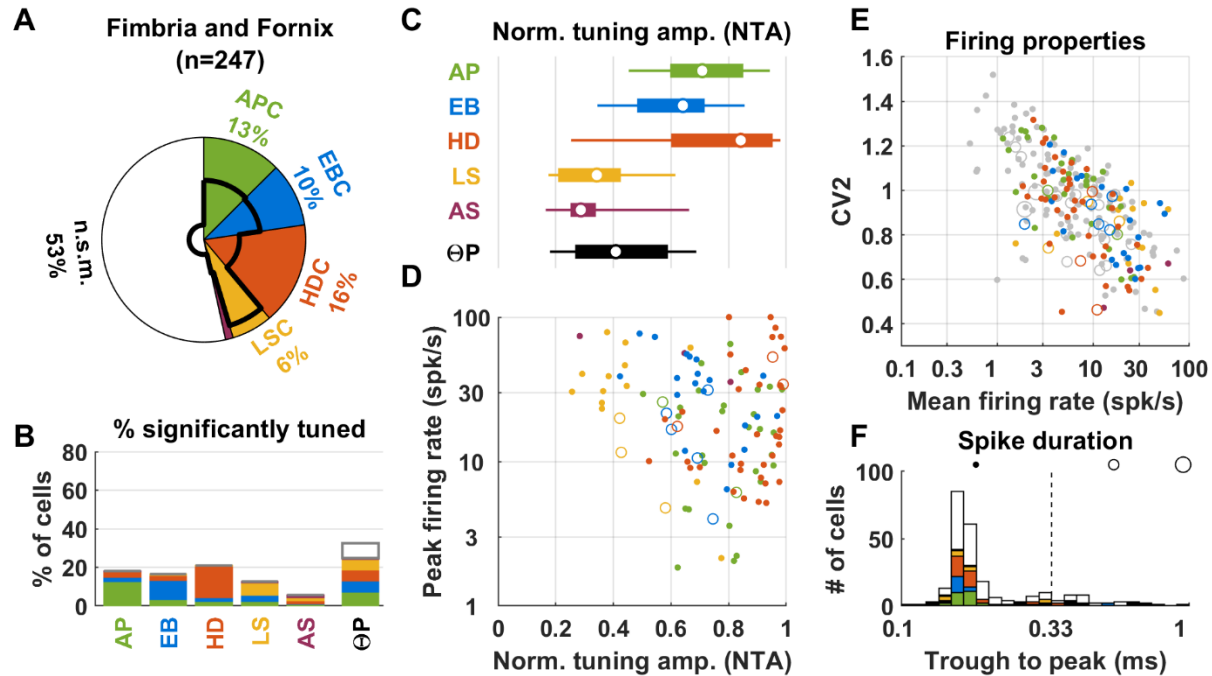
999 Finally, we note that some studies require HD cells to pass a threshold, i.e. $|R| \geq 0.26$ in (Jacobs et al.
1000 2017) or $|R| \geq 0.4$ (Yoder et al. 2009; Kornienko et al. 2018). Based on panel A, we estimate that
1001 $|R| \geq 0.26$ corresponds to $NTA \geq 0.67$ (broken lines in G-I). When this threshold is added to the shuffling
1002 test, a total of 223 cells are classified as HD-tuned, out of which 192 (86%) are also classified as HD-
1003 tuned by the LN model. However, this test now rules out 137 out of 329 cells (42%) that are classified as
1004 HD-tuned by the LN model, including, in particular, most (77/91, 85%) cells identified as APC or EBC with
1005 significant HD tuning by the LN model. Thus, using a threshold allows selecting well-tuned HD cells in a
1006 conservative manner, but tends to miss weaker HD cells and multimodal cells.



1007

1008 **Supplemental Figure 12: Recordings in the hippocampus of individual mice. Same legend as in Suppl.**

1009 **Fig. 2.**



1010

1011 **Supplemental Figure 13: Population responses in the fimbria and fornix.** Same legend as in Fig. 6. A
1012 summary of population responses follows.

1013 *APC:* A fraction (13%) of cells recorded in the fimbria and fornix were classified as APC (panels A,B). APC
1014 in the fimbria exhibited large NTA (panels C,D, median = 0.81, 1st-9th decile: 0.62-0.95); as well as large
1015 peak firing rate (median 16 spk/s, 1st-9th decile 3-36 spk/s; D).

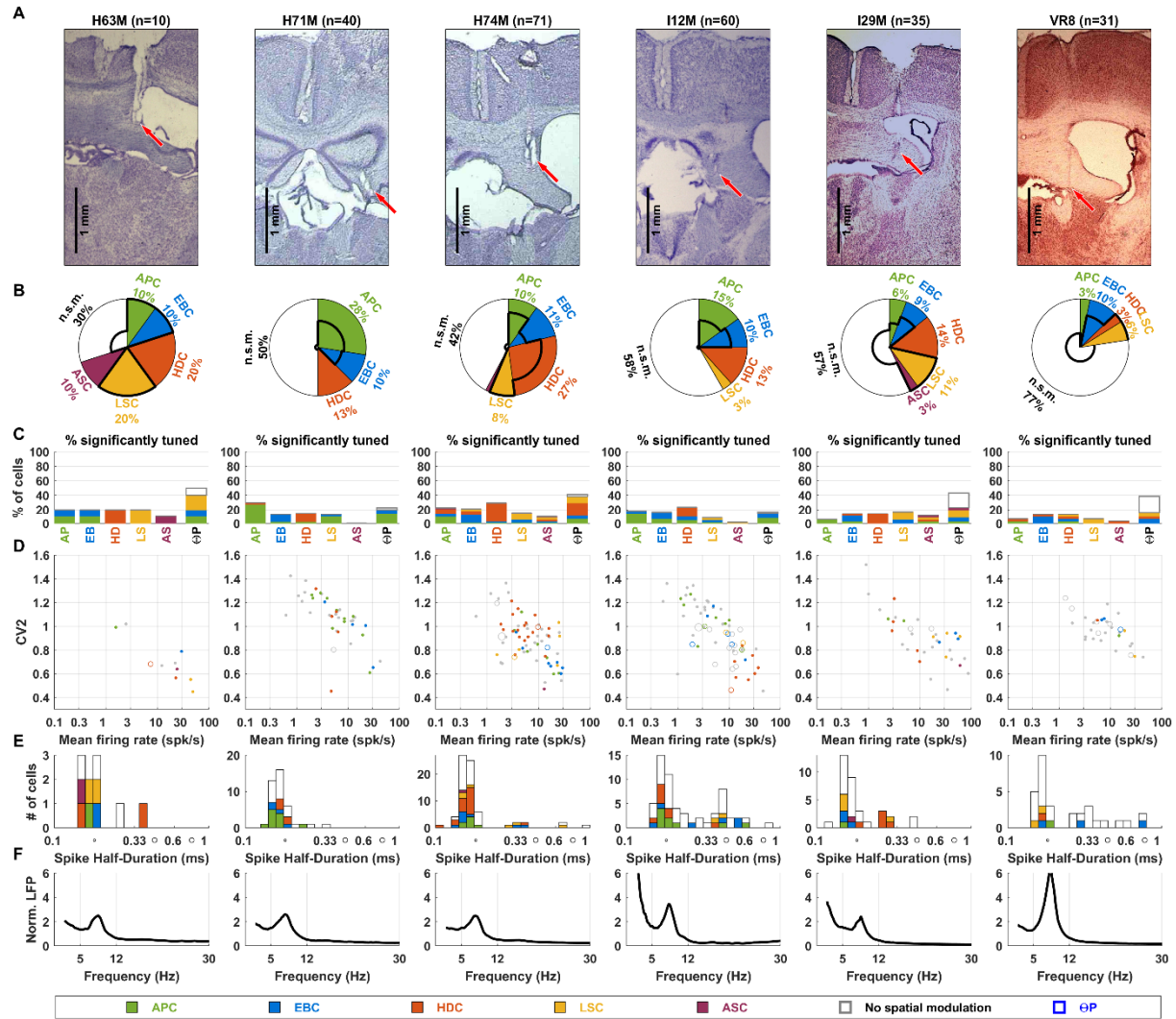
1016 *HDC:* A fraction (16%) of cells recorded in the fimbria and fornix were HDC (panels A,B). The median NTA
1017 was high (panels C,D; median: 0.91, 1st-9th decile 0.65-0.98) and similar as in ATN and cingulum (p=0.49
1018 and p=0.62 respectively). The median peak firing rate (16 spk/s; 1st-9th decile: 6-73) was similar to the
1019 value observed in the ATN (p=0.33, Wilcoxon rank sum test) and cingulum (p=0.7).

1020 *Other cells:* We also encountered a sizeable fraction of EBC (10%, panel A) that had large NTA (median
1021 0.69, range 0.54-0.9), similar to RSC (p=0.17); as well as a fraction of LSC (6%) with moderate NTA
1022 (median 0.42, 1st-9th decile: 0.3-0.69) similar to hippocampal LSC (p=0.12).

1023 *Theta rhythm:* Across the entire population of recorded neurons, 32% of fimbria neurons were ΘP
1024 modulated. However, this fraction increased to 53% when only spatially modulated neurons were
1025 considered.

1026 *Spiking properties:* Mean firing rate and CV2 were inversely correlated, as in other regions (panel E,
1027 Spearman rank correlation=-0.65, p<10⁻¹⁰). Most cells (86%) had short duration spikes, as expected from
1028 recordings performed in the white matter.

1029

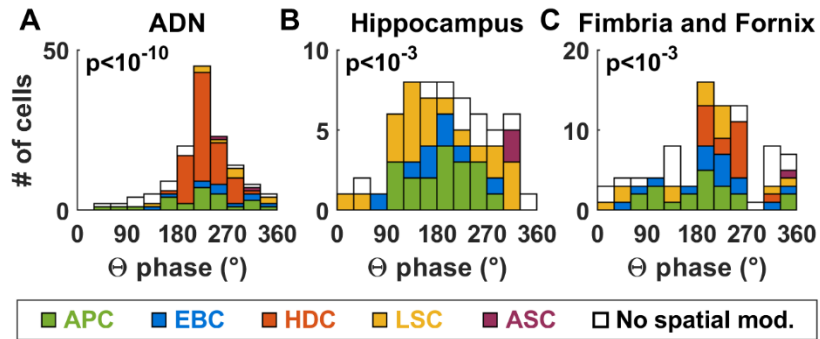


1030

1031 **Supplemental Figure 14: Recordings in the fimbria and fornix of individual mice. Same legend as in**
 1032 **Suppl. Fig. 2.**

1033

1034



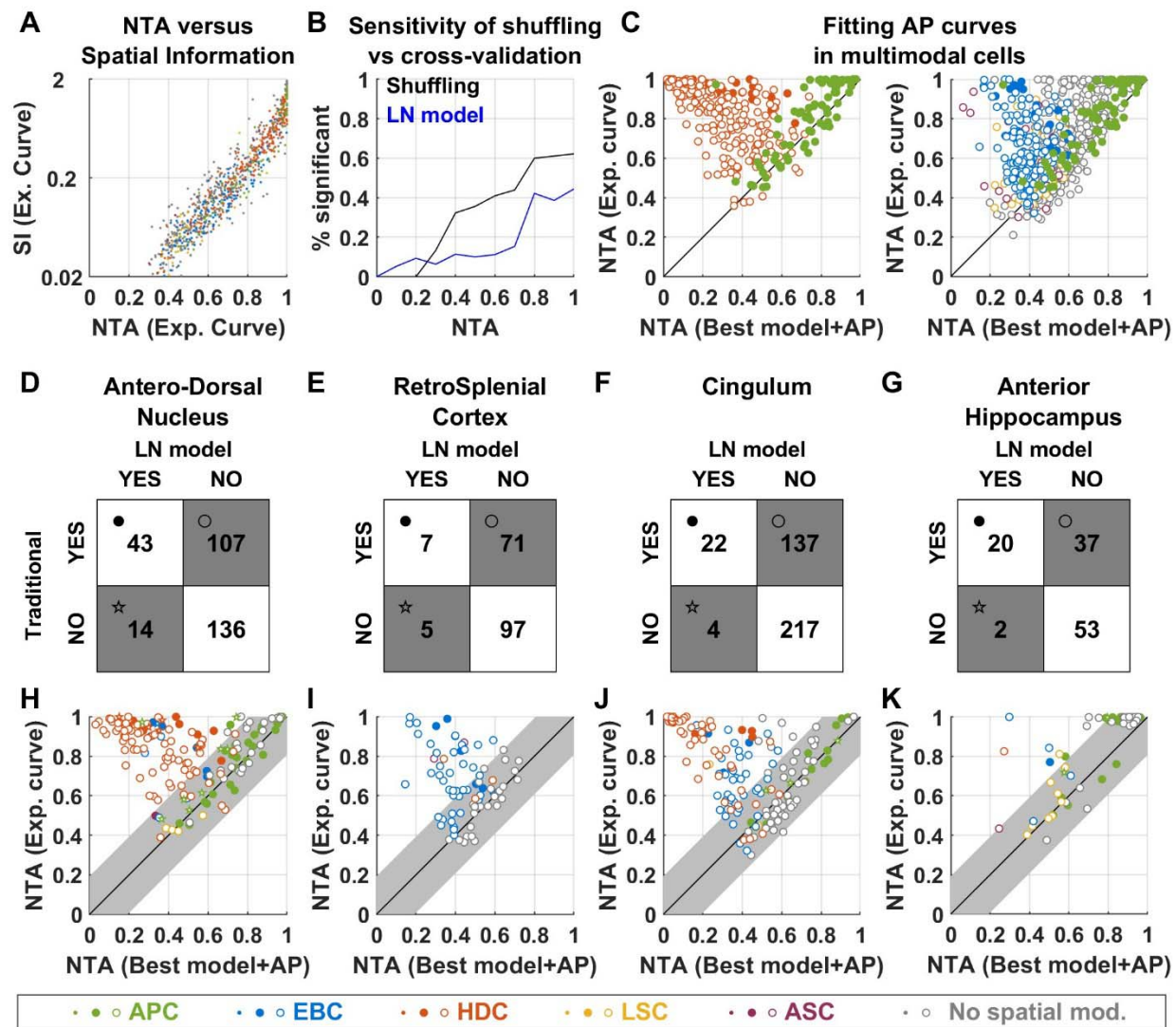
1035

1036 **Supplemental Figure 15: Distribution of preferred phase of Θ P-modulated cells.** Distributions are
1037 shown as histograms, where phases of 0, 90, 180 and 270 $^{\circ}$ correspond to the trough, ascending phase,
1038 crest and descending phase of the LFP. Cells are color-coded based on their classification.

1039 About half of ATN and hippocampal cells, and half of spatially-modulated neurons recorded in the
1040 fimbria, responded preferentially at a certain phase of the Θ -band LFP. We found that the distributions
1041 of preferred phase were non-uniform. In ATN (**A**), most cells responded preferentially during the
1042 descending phase (180-360 $^{\circ}$), with an average preferred phase of $230 \pm 10^{\circ}$. In particular, the two main
1043 classes of Θ P-modulated ATN neurons, HDC and APC, had an identical average preferred phase (230 vs
1044 235 $^{\circ}$, $p=0.7$, Watson-Williams test). In the hippocampus (**B**), the average preferred phase was $193 \pm 29^{\circ}$
1045 amongst APC, whereas preferred phases were distributed uniformly amongst LSC (yellow). In the fimbria
1046 (**C**), HDC responded preferentially in the descending phase ($238 \pm 20^{\circ}$) whereas APC fired closer to the
1047 LFP crest $184 \pm 40^{\circ}$ ($p=5.10^{-4}$ versus ATN, Watson-Williams test).

1048

1049



1050

1051 **Supplemental Figure 16: Classification of AP cells using the LN model versus traditional approaches.**

1052 We now follow the same logic as in **Suppl. Fig. 13** to analyze how the statistical approach used to classify
 1053 AP cells in the LN model differs from traditional techniques, where AP tuning is quantified by spatial
 1054 information (SI) of the tuning curve, and where a give SI value is considered significant if it is larger than
 1055 99% of a set of shuffled values (Skaggs 1993; Rubin et al. 2014). We consider data from the ATN,
 1056 cingulum and anterior hippocampus only (where most AP-tuned cells are found).

1057 **A:** Comparison between spatial information (SI), and the NTA measure used in this study. We plot the SI
 1058 and NTA of the experimental tuning curves of all cells (regardless of whether they were significantly
 1059 tuned to AP). Most data points cluster tightly to form a curve, indicating that there is a close
 1060 correspondence between SI and NTA. Cells are color-coded based on the classification by the LN model
 1061 (see legend).

1062 **B:** Comparison between the sensitivities of the cross-validation and shuffling tests, as in **Suppl. Fig. 13B**.
1063 Even when NTA is high (>0.8), only ~60% and ~40% cells pass the shuffling or cross-validation test,
1064 respectively. This indicates that apparently high AP tuning may occur randomly; but that these
1065 occurrences will be classified as non-significant based on both the shuffling test or LN model. This didn't
1066 occur with HD tuning (**Suppl. Fig. 13B**): this difference may be due to the fact that repetitively covering
1067 the 2D surface of the arena, which is required to archive statistical robustness, is harder than covering
1068 the 1D space of head direction. Similar to HD tuning, we find that the cross-validation procedure is
1069 generally less sensitive than the shuffling test for intermediate NTA.

1070 **C:** In multimodal cells, responses to variables other than AP (e.g. HD) can be erroneously interpreted as
1071 AP tuning using the traditional analysis. We plot the NTA of the experimental AP curve versus the NTA of
1072 the AP curve fitted by the LN model. For readability, we separate this panel in two plots, with HD cells
1073 and AP cells on the left and AP cells and other cell types on the right. Filled/open symbols represent cells
1074 that are HD tuned/not tuned based on the full LN model. Cells are color-coded based on the
1075 classification by the LN model (see legend). We find a striking number of HD cells (red) converging
1076 towards the upper left corner, i.e. where AP tuning appears very strong if HD tuning is not accounted for
1077 first. Thus, as pointed out by previous studies (Peyrache et al. 2017), HD cells may easily be confounded
1078 for AP cells. We also find that AP tuning is often overestimated in EB cells (blue).

1079 **D-G:** Contingency matrices indicating the number of cells classified as AP-tuned or not by the LN model
1080 and shuffling method in ATN (D), RSC (E), cingulum (F) and anterior hippocampus (G). We first note that
1081 most cells that were classified as AP-tuned by the LN model are also classified as AP-tuned by the
1082 shuffling test (ATN: 43/57, i.e. 75%; cingulum: 22/26, i.e. 85%; hippocampus: 20/22, i.e. 91%). This
1083 validates our finding that the ATN and cingulum contain APC populations. Next, we observe that the
1084 ATN, RSC and cingulum contain large fractions (36%, 39% and 36% respectively) of cells that are
1085 incorrectly classified as AP-tuned by the shuffling test only (open circles).

1086 **H-K:** As in **Suppl. Fig. 13G-I**, we plot the NTA of the experimental AP curve versus the curve fitted by the
1087 LN model. Cells tuned based on both classifications are shown as filled symbols. Cells tuned based on
1088 the shuffling/cross-validation methods only are shown as open disks/stars. Cells are color-coded based
1089 on the classification by the LN model (see legend). We draw a confidence interval, with a width
1090 estimated at 0.14 (based on cells classified as APC by both methods) around the diagonal.

1091 In the ATN (panel H), 68 cells are incorrectly classified as AP-tuned based on the shuffling procedure
1092 only and positioned above the confidence interval. Most of these cells (63/68) are HD cells (open orange
1093 circles). In the RSC (panel I), we also find a large group cells above the confidence interval, most of which
1094 (26/29) are EBC (open blue symbols). Thus, 32% (26/81) of RSC EBC would be erroneously characterized
1095 as APC. We also find a sizeable group of open symbols within the confidence interval (42 cells, i.e. 59%
1096 of cells classified as AP based on the shuffling method only). This suggests that a population of cells with
1097 weak but significant AP tuning, that would not have been detected by the LN model, may exist in the
1098 RSC. In the cingulum (panel J), we find 45% of HDC and 40% of EBC above the diagonal; as well as a
1099 group of cells within the confidence interval (47% of cells classified as AP based on the shuffling method
1100 only). These results are in line with the hypothesis that cingulum carries a mixture of ATN and RSC

1101 signals. In total, 68/300 (23%) ATN cells, 29/137 (16%) RSC cells and 72/380 (19%) cingulum cells, placed
1102 above the diagonal, were incorrectly classified as AP-tuned by the shuffling test.

1103 In the hippocampus (panel K), most (30/37) open symbols falls within the confidence interval.
1104 Furthermore, many cells cluster at the upper right corner of the graph, indicating that they are highly
1105 tuned to AP even when this tuning is overestimated by the experimental curve. This indicates that most
1106 cells identified by the shuffling test may be genuine AP cells, and that the LN model may have lacked the
1107 sensitivity to identify them. A possible remedy for this lack of sensitivity could be to perform longer
1108 recording sessions.

1109

1110 **Supplemental Movie 1: Response of a RSC EBC (same as in Fig. 5) during free exploration.** The movie
1111 shows the animal's motion and neuronal activity recorded during two minutes of free exploration.
1112 **Upper left panel:** animal motion from an allocentric point of view. The arena's boundary is shown in
1113 white, with the cue card represented as a dark gray arc. As time elapses, the animal's trajectory (light
1114 blue) and neuronal spikes (red dots) are shown. The arrow indicates the position of the nearest wall. The
1115 **right panel** displays exactly the same image, except for the light blue trajectory and red dots. The image
1116 is rotated in order to appear in egocentric coordinates. The light blue trajectory and red dots now
1117 represent the trajectory of the nearest boundary in egocentric coordinates. Spikes concentrate in front
1118 of the head, indicating that the neuron responds when the head is close to the wall and faces it. Lower
1119 left panel: raw neuronal data.

1120 **Supplemental Data 1:** Classification and response of all cells included in this study. Data is organized as a
1121 spreadsheet. For each cell, we provide the NTA and peak response to all variables (values are set to -1
1122 for variables that don't modulate the cell significantly), as well as the cell's mean firing rate, CV2 and
1123 trough to peak spike duration.